Modeling of spillage and debris floods as Newtonian and Viscoplastic Bingham flows with free surface with mixed stabilized finite elements

Elvira Moreno[a], Narges Dialami[b,*] and Miguel Cervera[b]

[a]Departamento de Ordenación de Cuencas, Ingeniería Forestal,
Universidad de los Andes, ULA, Vía Chorros de Milla, 5101, Mérida, Venezuela;
ElviraMoreno25@gmail.com (E. Moreno)
[b]International Center for Numerical Methods in Engineering (CIMNE),
Technical University of Catalonia (UPC),
Edificio C1, Campus Norte, Jordi Girona 1-3, 08034, Barcelona, Spain;
Narges.Dialami@upc.edu (N. Dialami); Miguel.Cervera@upc.edu (M. Cervera)
* Correspondence: Narges.Dialami@upc.edu; Tel.: +34 93 401 6529

ABSTRACT

This work deals with the numerical modeling of spillage and debris floods as Newtonian and viscoplastic Bingham flows with free surface using mixed stabilized finite elements. The main objective is the determination of the location of the free surface of the flow. A mixed stabilized velocity/pressure finite element formulation is used and the Orthogonal Subgrid Scale stabilization (OSS) and the Split Orthogonal Subgrid Scale stabilization (Split-OSS) techniques enable equal order interpolation for velocity and pressure. A double viscosity regularized Bingham model is introduced as an alternative to the regularized Papanastasiou model. The analytical solution to a Poiseuille flow has been obtained and a convergence test has been performed to compare both models. A simplified Eulerian method solved on a fixed mesh is presented to track the movement of the free surface. This is done by transporting the free surface with a stabilized level set method. The numerical solutions are compared with analytical, experimental results and numerical benchmarks from the literature. They are also compared with field data in a real case study, the flow due to the failure of a mining reservoir, which is solved in 3D and as a 2D simplified model.

Keywords*: Bingham flow, Split-Orthoghonal Subgrid Scale Stabilization, Level Set Method, Free Surface, Extrusion flow, Dam-Break Problem, Poiseuille flow, analytical solution*

1 INTRODUCTION

Dam-breaking resulting in spillage and debris floods is a classic problem of flow with free surface. The main objective is to study the behavior of the flow front or the front wave, determined by the free surface.

The flows due to the dam-break have increased their destructive power over human life as populations have been settled in the flood zones. An example of the flows due to the dam-break is the one produced by the rupture of the "El Guapo" dam during the torrential rains that hit Venezuela in December 1999. Likewise, this type of disaster has occurred in countries such as the United States, Japan and China, among others [1]. In recent times there has been an increased concern to ensure security against dam failure, as the flows composed of geological material can be considered as one of the most frequent and most destructive of all the geomorphological processes.

Mining waste flows can have the same impact as these geomorphological processes. The flows of displaced mining waste can cause catastrophic disasters depending on the location and the area where the event takes place. For dams located in high mountain areas, the displaced volume due to breakage reaches speeds much greater than the flow due to breakage of dams located in flat areas and cause greater damage. An example of this is the failure of the gypsum waste dam in Texas, United States, in 1966 [1], in which there was no significant impact due to its location. In other cases, such as the failure of the dam for fluorite wastes in Val di Stava, in 1985, produced 268 deaths. The dam breakage for heavy material waste in Los Frailes, Aznalcóllar, Spain, in 1998 [1, 2, 3], affected agricultural land, crops and water wells. The failure of the dam for manganese waste in the city of Mianyang, China, in 2011 [1, 4], as a result of heavy rains, affected 272 people who had to leave the site and a total of 200,000 people were left without water sources.

In the flow problem due to the dam-break, it is essential to predict the flow displacement path and the extent of the flood zone. With this information, flood maps can be prepared and emergency plans can be established in order to take preventive measures, such as early warning, and even mitigation measures in order to reduce the effects of the displacement of discharged materials.

Analytical solutions to determine the profile of the free surface and the velocity of the flow front are derived from the application of the shallow waters or Saint-Venant equations. The solution to the problem of instantaneous dam breakage was initially proposed by Barré de Saint-Venant in 1871 for a semi-infinite water tank, an initial downstream water depth of the dam, ideal fluid and horizontal channel. This solution is also valid for a downstream dry channel.

Ritter [5] solved the profile of the wave or of the free surface by means of the method of characteristics, considering ideal fluid (without viscosity) and no friction at the base. Stoker [6] proposed a similar solution to Ritter's in his classic book "Water wave" which was later generalized by Mangeney et al [7]. This solution considers the friction at the base of the channel on which the flow is displaced. The general solution of Mangeney is used for avalanches of detritus, snow or landslides. In floods, no friction should be taken into account.

Both the experimental observations and the data from the prototype made to assess the breakage of the Malpasset dam [8] have shown that the flow front due to instantaneous dam breakage propagates much more slowly than the predictions for an ideal fluid and that the front has a rounded shape. Therefore, the Ritter solution is not valid to predict the properties of the flow in this area.

In these observations, the flow corresponds to the Ritter solution from the zone where the upstream wave starts to the area considered to be dominated by the resistance to the displacement of the flow or wave tip region.
Under these considerations, Chanson et al. [9] proposes a diffusive wave model for a horizontal channel with friction at the base and zero initial velocity. It considers that the resistance of the flow in this zone is dominant and the acceleration and inertial terms are negligible.
In all these classical studies, the fluid is considered as Newtonian. However, this is a crude approximation for most debris flows, as they contain nonhomogeneous distributions of solids within a liquid. Depending on whether the shearing force tends to maximize or minimize interactions between the solid particles, the flow can exhibit non-Newtonian flow with either shear thinning or shear thickening properties. This loss of linearity between the shear strain rate and the stress is typical of non-Newtonian viscoplastic flows and, if a definite yield stress can be identified, Bingham fluids.
Viscoplastic materials are present in nature, industry and in a variety of processes. This motivates the interest in modeling them appropriately since Eugene Bingham [10] defined them rheologically for the first time in 1919, when he studied the behavior of paints. The viscoplastic models commonly used are the Bingham model [10] and the Herschel-Bulkley model [11].
These materials are characterized because they need a minimum shear stress to start moving. The presence of zones that move like rigid masses with constant velocity and others that move at different velocities is evident in experimental trials ([12], [13], [14]).
The most important properties of any fluid are density and viscosity. In confined flows, the variables to be determined are mainly velocities and pressure; in flows with free surface, it is necessary to determine, in addition, the position of free surface itself. Flows with free surface can develop in open channels and on the terrestrial surface. They may have Newtonian behavior, but in most cases, they present non-Newtonian behavior. They may have a laminar or turbulent character. A viscoplastic non-Newtonian rheology may be sufficient for the interstitial fluid phase of a debris flow, consisting of water with fine particles in suspension ([15], [16]). It may also be appropriate for other fluidized fine-grained soils, such as mudflows and flow slides in sensitive clays [17].
The problem of viscoplastic flows with free surface appears in many applications. The extrusion of a viscoplastic fluid to the atmosphere is one of them. Its applications include the industry of plastics, paints and synthetic fibers, as well as the lining of cables, the formation of transparent plastic films, ink injection and many others.
In the mold filling, Wang et al. [18] and Borzenko et al. [19] have simulated the non-Newtonian flow with free surface. However, in these works the data on the flow structure and free surface position is sparse.
Borzenko et al. [20] reproduced numerically non-Newtonian fluid flow with free surface occurring while filling of a plane channel in the gravity field. They presented flow separation into one and two dimensional zones. They discovered that the viscoplastic flows are portrayed by the existence of the unyielded areas in the flow.
Nikitin et al. [21] presented for dam-break problem, a numerical method in order to simulate free surface flow of Herschel-Bulkley fluids using a dynamically adapted octree meshes.
In a previous work [22], different types of confined flows for viscoplastic fluids of Bingham and Herschel-Bulkley have been studied in non-inertial and inertial cases with mixed P1/P1 finite elemnets stabilized with orthogonal subgrid scale. The regularized models of Bingham and Herschel-Bulkley proposed by Papanastasiou [23] have been

used. These studies have allowed to assess the behavior of these flows through the determination of the yield and unyielded zones, the yield surface and the characteristic variables of the flow.

The present work extends that numerical procedure to the modeling of viscoplastic flows with free surface, where the main objective is the determination of the location of the free surface of the flow. To this end, several elements are needed in the computational model: the constitutive model for the fluid, the movement of the fluid, the location and the movement of the free surface.

Regarding the constitutive model for the fluid, regularized Bingham models are used, namely the Papanastasiou model and a double viscosity (DV) model proposed here. The Navier-Stokes equations representing the movement of the fluid are solved using the stabilized model of reference [22], enhanced by the use of a split Orthogonal Subgrid Scale Method stabilization [24], more apt to the solution of problem with immiscible fluids and better numerical performance than the original OSS. A convergence test on a Poiseuille flow is performed to show the advantages of the double viscosity regularized Bingham model. To do this, the analytical solution to the problem has been obtained.

In order to locate the free surface in a fixed mesh, the Level Set Method is used. This requires the solution of a stabilized transport equation. The coupling of the movement of the fluid and the free surface is done in a staggered manner following a simplified Eulerian procedure.

The paper is outlined as follows. Regularized Bingham models are presented in Section 2. The governing Navier-Stokes equations and their discrete counterparts are given in Sections 3 and 4 respectively. Sections 5 and 6 describe the problem of flows with free surface and their numerical solution. The analytical solution for a Bingham Fluid Poiseuille flow is obtained in Section 7 and a convergence test is reported. Three numerical solutions are presented to apply the developed numerical procedure: extrusion flow with free surface, Newtonian and viscoplastic flows (Section 8), spillage of water and oil due to dam-break, Newtonian flow (Section 9), failure of a mining reservoir, a real case solved as a 2D simplified model and in 3D (Section 10). The numerical solutions are compared with analytical solutions and experimental and numerical results of other authors. They are also compared with field data in the real case. Section 11 presents the conclusions of the work.

2 REGULARIZED VISCOPLASTIC BINGHAM MODELS

Eugene C. Bingham described the behavior of paints with this model in 1919, published in his book "Fluidity and Plasticity" [10]. The model was analyzed by Oldroyd [25], Reiner [26] and Prager [27]. Paints, grouts, toothpaste, sludge, some drilling fluids and food substances such as margarine, mayonnaise and ketchup are good examples of Bingham plastics [23].

Bingham plastics require a yield stress, τ_y, to be surpassed to begin to move. Therefore, the deviatoric stress tensor is

$$\begin{aligned} \boldsymbol{\tau} &= 2\left(\mu_0 + \frac{\tau_y}{\dot{\gamma}}\right)\boldsymbol{\varepsilon}(\mathbf{u}) && \tau > \tau_y \\ \dot{\gamma} &= 0 && \tau \leq \tau_y \end{aligned} \tag{2.1}$$

where μ_0 is the plastic viscosity, τ is the equivalent deviatoric stress and $\dot{\gamma}$ is the equivalent strain rate. To determine if a particle of the fluid moves or not, whether the

equivalent deviatoric stress, τ, exceeds the value of the yield stress, τ_y, is checked. If $\tau > \tau_y$, the behavior is similar to a Newtonian fluid; otherwise, the fluid does not flow.
In the Bingham model the apparent viscosity is given by:

$$\begin{aligned} \mu(\dot{\gamma}) &= \mu_0 + \frac{\tau_y}{\dot{\gamma}} & \tau &> \tau_y \\ \dot{\gamma} &= 0 & \tau &\leq \tau_y \end{aligned} \tag{2.2}$$

Note that the apparent viscosity $\mu = \mu(\dot{\gamma})$ decreases with the increase in equivalent strain rate. As can be seen in Equation (2.2), the apparent viscosity is not bounded when the deformation rate tends to zero $\left(\lim_{\dot{\gamma}\to 0} \mu \to \infty\right)$. This is not a limitation in analytical solutions for simple problems, but it is a serious hindrance in computational approaches ([23], [28]). To avoid this drawback, regularized models are usually adopted.
Papanastasiou [23] proposed a regularization of the apparent viscosity so that the yielding and unyielding behavior is described with one single expression, via a smooth function that depends on of the deformation rate and a regularized parameter, m, in the form:

$$\mu(\dot{\gamma}) = \mu_0 + \frac{\tau_y}{\dot{\gamma}}(1 - \exp(-m\dot{\gamma})) \tag{2.3}$$

Note that m [s] is a regularized relaxation time. Figure 1 shows the influence of the regularization parameter m.

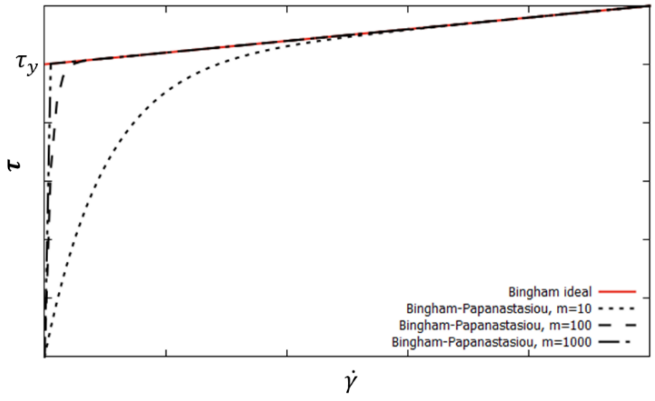

Figure 1. Papanastasiou's regularization of Bingham's model.

When the strain rate tends to zero, the viscosity tends to $\mu_{\max} = \lim_{\dot{\gamma}=0} \mu(\dot{\gamma}) = \mu_0 + m\tau_y$.
The same regularization procedure was applied to the Hershel-Bulkley model (Mitsoulis and Zisis [29], Frey et al. [30], Perić and Slijecpčević [28]).
Souza Mendes and Dutra [31] proposed an alternative exponential regularization (SMD):

$$\mu(\dot{\gamma}) = \left(\mu_0 + \frac{\tau_y}{\dot{\gamma}}\right)(1 - \exp(-m\dot{\gamma})) \tag{2.4}$$

so that the viscosity is bounded by a value $\mu_{\max} = \lim_{\dot{\gamma}=0} \mu(\dot{\gamma}) = m\tau_y$ at the origin. Note that for large values of the regularization parameter m Equations (2.3) and (2.4) are effectively identical.

Inspired by this, a double-viscosity (DV) linear regularized Bingham's model is used in this work. A regularization viscosity, $\mu_r = m\tau_y$, is defined in terms of the regularization parameter m (Figure 2), so that

$$\mu(\dot{\gamma}) = \begin{cases} \mu_0 + \dfrac{\tau_y}{\dot{\gamma}} & \dot{\gamma} > \dot{\gamma}_c \\ \mu_r & \dot{\gamma} \leq \dot{\gamma}_c \end{cases} \tag{2.5}$$

where the value of the critical deformation rate $\dot{\gamma}_c$ is given by:

$$\dot{\gamma}_c = \frac{\tau_y}{\mu_r - \mu_0} \tag{2.6}$$

Note the critical stress τ_c corresponding to the critical viscosity

$$\tau_c = \tau_y \frac{\mu_r}{\mu_r - \mu_0} > \tau_y \tag{2.7}$$

is higher than the yield stress τ_y, as shown in Figure 2. This difference vanishes for increasing values of m.

Figure 3 shows the comparison between the Papanastasiou, the SMD and the DV models for different values of the regularization parameter m; the values yielding stress $\tau_y = 10$ Pa and viscosity $\mu_0 = 2$ Pa.s have been considered.

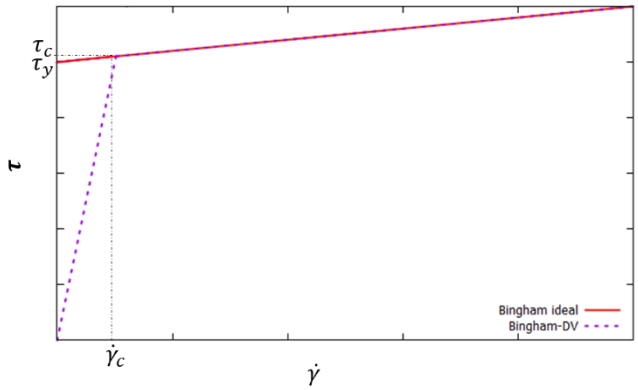

Figure 2. Ideal Bingham and Bingham-DV models.

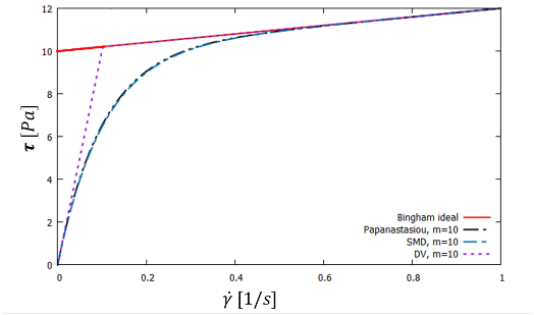

(a)

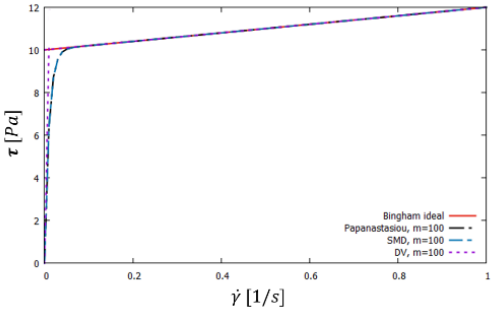

(b)

Figure 2. Comparison between ideal and regularized Bingham models.
(a) m = 10, (b) m = 100

The convergence study in Section 7 shows that the DV linear model is a better approximation to the ideal Bingham model than the exponential alternatives in terms of the L2 norm of the error in velocity.

3 GOVERNING EQUATIONS

The continuum problem of incompressible and isothermal fluid dynamics can be solved considering the Navier-Stokes equations. The Navier-Stokes equations, initially applied for Newtonian fluids, can be used in conjunction with the rheological viscoplastic models of (regularized) Bingham fluids as the constitutive equation.
The Navier-Stokes problem for incompressible fluids consists in finding the velocity **u** and pressure p such that the momentum balance equation is satisfied. Using an Eulerian description for an incompressible fluid moving in a bounded domain Ω with the contour $\Gamma = \partial\Omega$ during a time interval $[0, T]$ is defined as

$$\rho(\partial_t \mathbf{u} + \mathbf{u} \cdot \nabla \mathbf{u}) - \nabla \cdot \boldsymbol{\sigma} = \mathbf{f} \tag{3.1}$$

where **f** is the external forces vector, $\boldsymbol{\sigma}$ is the stress tensor and ρ is the fluid density. The incompressibility condition of the fluid in Ω, $[0, T]$ is

$$\nabla \cdot \mathbf{u} = 0 \tag{3.2}$$

Decomposing the stress tensor into its volumetric and deviatoric parts reads

$$\boldsymbol{\sigma} = -p\mathbf{I} + \boldsymbol{\tau} \tag{3.3}$$

where **I** is the identity tensor and τ is the deviatoric part of stress tensor. For a Newtonian fluid, using the Stokes hypothesis and considering the incompressibility condition, the deviatoric part of stress tensor is expressed as

$$\boldsymbol{\tau} = 2\mu\boldsymbol{\varepsilon}(\mathbf{u}) \tag{3.4}$$

where μ is the dynamic viscosity (constant in the case of a Newtonian fluid) and $\boldsymbol{\varepsilon}(\cdot)$ is the symmetric gradient of the velocity.
Therefore, equation (3.1) can be rewritten in terms of velocity **u** and pressure p as

$$\rho(\partial_t \mathbf{u} + \mathbf{u} \cdot \nabla \mathbf{u}) - \nabla \cdot \boldsymbol{\tau} + \nabla p = \mathbf{f} \tag{3.5}$$

The boundary conditions are

- Dirichlet condition
$$\mathbf{u} = \overline{\mathbf{u}} \text{ on } \partial\Omega_{\mathrm{d}}, [0, T],$$
- Neumann condition
$$\mathbf{n} \cdot \boldsymbol{\sigma} = \mathbf{t} \text{ on } \partial\Omega_{\mathrm{n}}, [0, T],$$
- Mixed conditions

$$\mathbf{u}\cdot\mathbf{n}=0$$
$$\mathbf{n}\cdot\boldsymbol{\sigma}\cdot\mathbf{g_1}=t_1$$
$$\mathbf{n}\cdot\boldsymbol{\sigma}\cdot\mathbf{g}_2=t_2 \text{ on } \partial\Omega_m,\ [0,\mathrm{T}],$$

where **n** is a unit vector normal to the boundary and $\partial\Omega_{\mathrm{d}}$, $\partial\Omega_{\mathrm{n}}$ and $\partial\Omega_m$ are Dirichlet, Neumann and mixed boundaries, respectively. Vectors $\mathbf{g}_1$ and $\mathbf{g}_2$ (in the 3D case) span the space tangent to $\partial\Omega_m$. The traction vector on the boundary with mixed condition is $\mathbf{t}=[t_1,t_2]$. Initial conditions need also to be specified.

Conditions at the bottom boundary of channels is often represented through a mixed boundary law known as *wall law*. Physically, this condition models the fact that the greater the roughness of the bottom surface, the larger the tractions and the lower the velocity. This is expressed as

$$\boldsymbol{t}=\rho\frac{U_*^2}{|\boldsymbol{u}|}\boldsymbol{u} \tag{3.6}$$

where ρ is the density and U_* is the solution of the nonlinear equation

$$\frac{|\mathbf{u}|}{U_*}=\frac{1}{k}\log\left(\frac{U_*\delta}{\upsilon}\right)+C \tag{3.7}$$

where k = 0.41 is the Von Karman constant, C = 5.5 is an integration constant, δ is the distance from the bottom where the velocity is evaluated and υ is the cinematic viscosity, $\upsilon=\frac{\mu}{\rho}$.

4 DISCRETE MODEL OF THE FLUID FLOW AND STABILIZATION

The governing equations are first discretized in time using a finite difference scheme and then a finite element approximation is used in space. This procedure uncouples the errors arising from the temporal and spatial discretization.

Temporal discretization is done by Backward Differentiation Formula (BDF1) [32]. In the spatial discretization, a mixed formulation (velocity/ pressure) of finite elements is used [33]. Equal order linear (and bilinear for quads) finite elements for both velocity and pressure are considered.

The weak form of the problem is obtained using a Galerkin technique and the nonlinear terms of the momentum equation (i.e. the convective and viscous terms of Equation (3.5)) are linearized using a secant Picard method.

The velocity **u** belongs to the velocity space $V\subset\left[H^1(\Omega)\right]^d$ of vector functions whose components and their first derivatives are square-integrable and the pressure p belongs to the pressure space $Q\subset L_2$ of square-integrable functions. Let $V_h\subset V$ and $Q_h\subset Q$ be the corresponding finite element approximation spaces.

Let $\boldsymbol{\Omega}\subset\mathbb{R}^d$ be the domain in a time interval [0, T], and Ω^e the elemental domain such that $\cup\boldsymbol{\Omega}^e=\boldsymbol{\Omega}$, with e = 1, 2,..., n_{el} where n_{el} is the number of elements. Given the velocity $\mathbf{u}_h^n$ at time t^n and the values of all variables in the iteration i-1 at time t^{n+1}, the standard Galerkin discrete problem consists in finding $\mathbf{u}_h^{n+1,i}\in V_h$ and $p_h^{n+1,i}\in Q_h$ such that

$$\int_{\Omega} \rho^{n+1,i} \frac{\boldsymbol{u}_h^{n+1,i} - \boldsymbol{u}_h^n}{\delta t} \cdot \boldsymbol{v}_h d\Omega + \int_{\Omega} \rho^{n+1} \left(\boldsymbol{u}_h^{n+1,i-1} \cdot \nabla\right) \boldsymbol{u}_h^{n+1,i} \cdot \boldsymbol{v}_h d\Omega$$
$$+ \int_{\Omega} 2\mu(\dot{\gamma})^{n+1,i-1} \nabla^s \boldsymbol{u}_h^{n+1,i} : \nabla^s \boldsymbol{v}_h d\Omega - \int_{\Omega} p^{n+1} \nabla \cdot \boldsymbol{v}_h d\Omega$$
$$= \int_{\Omega} \boldsymbol{f}^{n+1} \cdot \boldsymbol{v}_h d\Omega + \int_{\Gamma_n} \boldsymbol{t}^{n+1} \cdot \boldsymbol{v}_h d\Gamma \qquad (4.1)$$
$$+ \int_{\Gamma_n} (t_1^{n+1} \boldsymbol{g}_1 + t_2^{n+1} \boldsymbol{g}_2) \cdot \boldsymbol{v}_h d\Gamma$$

$$\int_{\Omega} q_h \nabla \cdot \boldsymbol{u}_h^{n+1,i} d\Omega = 0 \qquad (4.2)$$

For iterations $i = 1, 2 \ldots$, until getting the convergence, that is, until $\mathbf{u}_h^{n+1,i} \approx \mathbf{u}_h^{n+1,i-1}$ in the specified norm.

Standard Galerkin finite element formulations of incompressible flows using equal interpolation for both the velocity and pressure fields do not meet the Ladyzenskaja-Babuška-Brezzi condition and need to be stabilized. The most commonly used stabilization procedures are based on subscale methods proposed by Hughes [34, 35]. These methods consist in decomposing the solution in two components, for example, for the velocity which is $\mathbf{u} = \mathbf{u}_h + \bar{\mathbf{u}}$; a component, $\mathbf{u}_h$, resolved in the scale of the finite element mesh and a subscale, $\bar{\mathbf{u}}$, that cannot be captured by the finite element partition and that is solved analytically. The specific approach used for the subscale defines the stabilization model.

In this work, the split Orthogonal Sub-grid Scale stabilization technique (split-OSS) is used. Proposed by Codina [24,36], this technique is a slight modification of the original OSS procedure ([37, 38]), and based in the well-known Algebraic Sub-Grid Scale (ASGS) method [34].

Let

$$\mathbf{R}_h = \int_{\Omega} [-\rho \mathbf{f} + \rho(\partial_t \mathbf{u}_h) + \rho(\mathbf{u}_h \cdot \nabla \mathbf{u}_h) - 2\mu(\dot{\gamma})(\nabla \cdot \nabla \mathbf{u}_h) + \nabla p_h] \mathrm{d}\Omega \qquad (4.3)$$

be the residual of the momentum equation. In the ASGS technique, the sub-scale, $\bar{\mathbf{u}}$, is taken proportional to $\mathbf{R}_h$, so that $\bar{\mathbf{u}} = -\tau_1 \mathbf{R}_h$, where τ_1 is a numerical parameter. Similarly, in the OSS technique, the sub-scale, $\bar{\mathbf{u}}$, is taken proportional to the orthogonal projection of the residual

$$\bar{\mathbf{u}} = -\tau_1 P_h^{\perp} \mathbf{R}_h = -\tau_1 (\mathbf{R}_h - P_h \mathbf{R}_h) \qquad (4.4)$$

where P_h is the projection onto the FE space and the corresponding orthogonal projection is $P_h^{\perp} = \mathbf{I} - P_h$. The OSS stabilization is less dissipative than alternative procedures.

In problems involving the interface between immiscible fluids the residual on integration points on opposite sides of the interface may vary abruptly because of

density difference and this may lead to the numerical errors. These are avoided by adopting a modified projection [39]:

$$P_{h\rho}(\boldsymbol{R}_h^{n+1}) = \rho P_h\left(\frac{\boldsymbol{R}_h^{n+1}}{\rho}\right) \tag{4.5}$$

In the split-OSS stabilization, separate projections are used for the different terms in the residual, because this leads to an improved numerical performance in large 3D problems.

Complementarily, the pressure subscale, $\overline{p}^{n+1}$, is taken proportional to the orthogonal projection of the residual of continuity equation (3.2):

$$\overline{p}^{n+1} = -\tau_2\left(\nabla\cdot\mathbf{u}_h^{n+1}\right) \tag{4.6}$$

where τ_2 is a numerical parameter.

The stabilization parameters τ_1 and τ_2 in Equations (4.4) and (4.6) are so defined to obtain a stable numerical scheme. Parameter τ_1 is calculated for each element as $\tau_1 = \left[c_1\frac{\mu}{h^2} + c_2\frac{\rho|\mathbf{u}^e|}{h}\right]^{-1}$, where h is the projection of the element in the flow direction and $|\mathbf{u}^e|$ is the norm of velocity in the element; c_1 and c_2 are two coefficients that are chosen as $c_1 = 4$ and $c_2 = 2$ ([37, 38]). Parameter τ_2 is $\tau_2 = \left(\frac{h}{\tau_1}\right)^2$. Using these parameters for *linear* elements, *optimal quadratic* and *linear* convergence rates are achieved for velocity and pressure, respectively, in the L_2-norm.

Consequently, the discrete linearized problem, stabilized with split-OSS, is finding $\mathbf{u}_h^{n+1}$ and p_h^{n+1} such that

$$\begin{aligned}\int_\Omega \Big[&\frac{\rho}{\delta t}(\boldsymbol{u}_h^{n+1} - \boldsymbol{u}_h^n)\cdot\boldsymbol{v}_h + 2\mu(\dot{\gamma})^{n+1,i}\nabla^s\boldsymbol{u}_h^{n+1}:\nabla^s\boldsymbol{v}_h + \rho\left(\boldsymbol{u}_h^{n+1}\cdot\nabla\boldsymbol{u}_h^{n+1,i}\right)\cdot\boldsymbol{v}_h \\ &- p_h^{n+1}\nabla\cdot\boldsymbol{v}_h - \boldsymbol{f}^{n+1}\cdot\boldsymbol{v}_h\Big]\,d\Omega \\ &+ \sum_e\int_{\Omega_e}\tau_1\rho(\boldsymbol{u}_h^{n+1}\cdot\nabla\boldsymbol{v}_h) \\ &\cdot[(\rho\boldsymbol{u}_h^{n+1}\cdot\nabla\boldsymbol{u}_h^{n+1}) - \rho P_h(\boldsymbol{u}_h^{n+1}\cdot\nabla\boldsymbol{u}_h^{n+1})]d\Omega \\ &+ \sum_{e=1}^{n_{el}}\int_{\Omega_e}\tau_2^{n+1,i-1}(\nabla\cdot\boldsymbol{v}_h)\left(\nabla\cdot\boldsymbol{u}_h^{n+1,i-1}\right)d\Omega = 0\end{aligned} \tag{4.7}$$

$$\begin{aligned}\int_\Omega\,&[q_h\nabla\cdot\mathbf{u}_h^{n+1}]\,\mathrm{d}\Omega \\ &+ \sum_e\int_{\Omega_e}\tau_1\nabla q_h\cdot\left[(\nabla p_h^{n+1} - \mathbf{f}^{n+1}) - \rho P_h\left(\frac{\nabla p_h^{n+1}}{\rho} - \frac{\mathbf{f}^{n+1}}{\rho}\right)\right]\mathrm{d}\Omega \\ &= 0\end{aligned} \tag{4.8}$$

For iterations $i = 1,2\ldots$ until getting the convergence, that is, until it gets $\mathbf{u}_h^{n+1,i-1} \approx \mathbf{u}_h^{n+1,i}$ and $p_h^{n+1,i} \approx p_h^{n+1,i-1}$ in the norm defined by the user.

5 FLOWS WITH FREE SURFACE

Flows with free surface are a particular case of the flows of two immiscible fluids. The free surface or interface (Γ_{int}) of the fluid of interest is in contact with the air, a fluid with much lower density and viscosity than the transported fluid. The free surface is in motion. These flows occur very frequently in industrial and also in environmental processes. The corresponding problem can be solved using the Navier-Stokes equations. Basically, two methods may be used in a fully Eulerian description:

1. The problem is solved considering the transported fluid (fluid 1) and the air (fluid 2) as a problem of two immiscible fluids. The Navier-Stokes equations are solved both in the domain of the fluid 1, Ω_1, and in the domain of the fluid 2, Ω_2, see Figure 4. At each point of the domain, the properties ρ and μ of the corresponding fluid are considered.
   Tractions should be continuous at the interface line. But when solved monolithically, there is continuity of the full stress tensor, so an excess of continuity (over-continuity) is spuriously imposed on the solution.

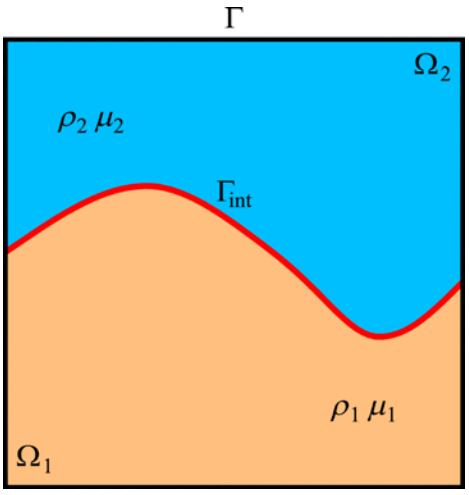

Figure 4. Boundary conditions for a fluid divided by the interface in method (1).

2. The effect of air (fluid 2) on the fluid of interest (fluid 1) is neglected, which simplifies the problem by uncoupling the two domains [39]. Therefore:

   a. The Navier-Stokes equations are solved in the fluid domain 1, Ω_1, with the properties $\mu = \mu_1$ and $\rho = \rho_1$. The natural boundary condition on the free surface (Γ_{int}) is zero traction in a weak form ($\boldsymbol{\sigma} \cdot \mathbf{n} = \mathbf{t} = \mathbf{0}$), see Figure 5a.

   b. The Navier-Stokes equations are solved in the fluid domain 2, Ω_2, with the properties $\mu = \mu_2$ and $\rho = \rho_2$. The free surface is considered a boundary with imposed velocity conditions, $\mathbf{u} = \bar{\mathbf{u}}$, obtained from the solution of fluid 1, see Figure 5b.

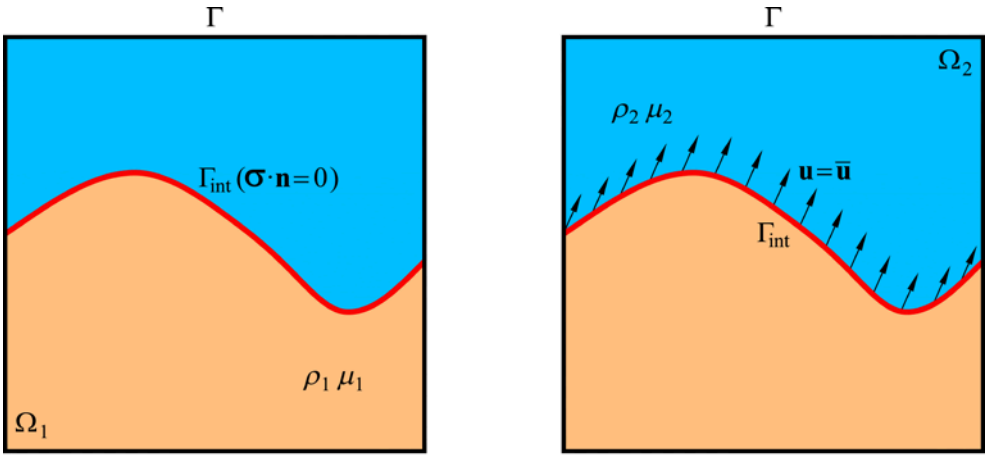

Figure 5. Boundary conditions for a fluid divided by the interface in the simplified method (2).

In both methods, the initial position of the free surface is known at time $t = 0$, as well as the properties of the fluid in each domain. Then, the movement of the free surface and its location are obtained from the velocities determined in the whole domain at any time t; the properties $\mu_{1,2}$ and $\rho_{1,2}$ must be assigned to the new domains Ω_1 and Ω_2. To determine this position and assign these properties, there are different methods. One of the most known and used methods to perform both tasks is the "level set" method [40, 41].

In this work, the simplified Eulerian model is adopted together with the "level set" method to solve the problem of flows with a free surface. A fixed mesh is used for solving the movement of both the fluid and the interface. This procedure has the following advantages:

- The decoupled solution is more efficient, as each fluid is solved independently.
- There is neither over-continuity of pressure nor tangential stress at the interface and, therefore, it is not necessary to adopt specific procedures.
- The free surface is subjected to the natural boundary condition ($\boldsymbol{\sigma} \cdot \mathbf{n} = \mathbf{t} = \mathbf{0}$) in the region of the fluid of interest.

6 MOVING FREE SURFACE BY THE LEVEL SET METHOD

6.1 THE LEVEL FUNTION

The level set method uses a continuous function defined over the whole domain Ω to determine the subdomains occupied by the transported fluid Ω_1 and by air Ω_2 ($\Omega = \Omega_1 \cup \Omega_2$). The method consists in propagating the interface, $\Gamma_{\text{int}}(t)$, fixed by the zero level of the continuous function ψ, so that $\psi > 0$ for domain Ω_1 and $\psi < 0$ for domain Ω_2. This function ψ can be defined as a distance function with a sign, $\psi(\mathbf{x}, t) = \pm d$, where d is the perpendicular distance from $\mathbf{x}$ to $\Gamma_{\text{int}}(t = 0)$.

The evolution of this function is given by the transport equation:

$$\frac{\partial \psi}{\partial t} + \mathbf{u} \cdot \nabla \psi = 0 \qquad (6.1)$$

Boundary conditions must be specified in the inflow boundary, to determine how each fluid enters the domain at all times. Additionally, the initial position of the interface needs to be defined:

$$\psi(\mathbf{x}, 0) = \psi_o(\mathbf{x}) \quad \text{in} \quad \Omega \tag{6.2}$$

The solution of the problems of flow with free surface is done in two steps, first, the Navier-Stokes equations are solved for a fixed position of the free surface and, second, Equation (6.1) is solved to transport the free surface with the previously computed velocity field.
Once the function ψ is determined at a given time, and the corresponding position of the free surface and the domain of each fluid is known, the mechanical properties are assigned to each fluid. Appropriate splitting and integration techniques are applied to those elements cut by the free surface.

6.2 DISCRETE MODEL OF THE LEVEL FUNTION

The weak form of Equation (6.1) is obtained by multiplying each term by an arbitrary element of $x \in X, X = L^2(\Omega)$. The problem is finding $\psi \in L^2(\mathrm{X})$ such that

$$\int_{\Omega} \partial_t \psi x d\Omega + \int_{\Omega} [\boldsymbol{u} \cdot \nabla \psi] x d\Omega \tag{6.3}$$

Temporal discretization by the Backward Differentiation Formula (BDF1) and spatial discretization by the finite elements method is used. Due to the pure convective type of Equation (6.1), the ASGS method is used to stabilize the discrete problem.
Consequently, the discrete problem is: given a velocity $\mathbf{u}_h^{n+1}$ at a time t^{n+1} and a function $\psi_h^n \in X_h$ at a time t^n, find $\psi_h^{n+1} \in X_h$ solving:

$$\begin{aligned} &\int_{\Omega} \frac{1}{\delta t} \psi_h^{n+1} x_h \mathrm{d}\Omega + \int_{\Omega} \mathbf{u}_h^{n+1} \cdot \nabla \psi_h^{n+1} x_h \mathrm{d}\Omega \\ &\quad + \sum_{e=1}^{n_{el}} \int_{\Omega^e} \tau^{n+1} (\mathbf{u}_h^{n+1} \cdot \nabla x_h) \left(\frac{1}{\delta t} \psi_h^{n+1} + \mathbf{u}_h^{n+1} \right. \\ &\quad \left. \cdot \nabla \psi_h^{n+1} \right) \mathrm{d}\Omega = 0 \end{aligned} \tag{6.4}$$

τ is a stabilization parameter, calculated in each element as:

$$\tau = \frac{h}{2|\boldsymbol{u}^e|} \tag{6.5}$$

where h is the projection of the element in the flow direction and $|\boldsymbol{u}^e|$ is the norm of velocity in the element.

6.3 REDEFINITION OF THE LEVEL FUNTION

During the evolution of the level set equation, the function ψ needs to remain as a signed distance function $|\nabla \psi| = 1$. To guarantee this, in this work the function ψ is redefined after computation according to the expression:

$$\psi = sgn(\psi^0)d \qquad (6.6)$$

where ψ^0 represents the calculated value of ψ, d is the perpendicular distance between the node under consideration to the front of the interface, and $sgn(\cdot)$ is the signum of the value enclosed in the parenthesis, see Figure 6. The redefinition of the function is only done in five node layers in each side of the interface.

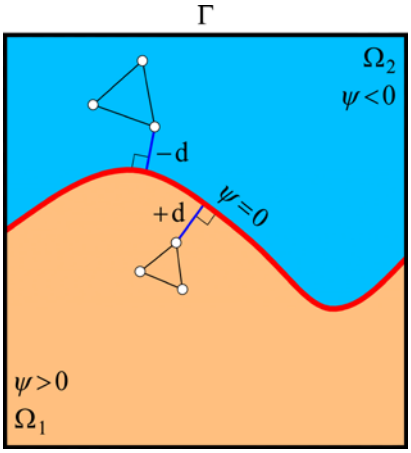

Figure 6. Distance from element nodes and the interface for two elements located in opposite sides of the interface.

6.4 COUPLING BETWEEN THE FLOW EQUATIONS AND THE LEVEL SET EQUATION

The Navier-Stokes equations (3.1)-(3.2) and the transport equation (6.1) are coupled. On the one hand, the properties of the fluid are necessary for calculating the velocity **u** and the pressure p depend on the values of level set function ψ. On the other hand, function ψ is transported by the velocity **u**.

In this work, the corresponding discrete equations are uncoupled by using the velocity computed at the previous time step $\mathbf{u}_h^n$ for the convection of the free surface. This uncoupling introduces a CFL restriction on the time step size so that the front does not advance more than one layer of elements in one time step.

6.5 NUMERICAL INTEGRATION OF THE ELEMENTS CUT BY THE INTERFACE

In order to satisfy the free surface condition ($\boldsymbol{\sigma} \cdot \mathbf{n} = \mathbf{t} = \mathbf{0}$) in the interface, located by the level set function, a modified integration rule is used in the elements cut by it, so that at each fluid phase is integrated exactly.

Figure 7 shows the modified integration rule in 2D. The intersected triangle is divided into triangular sub-elements so that the interface coincides with a face of two sub-elements. In this face the interface condition is imposed. For each sub-element the same integration rule as for the uncut elements is used. A similar procedure is used in 3D.

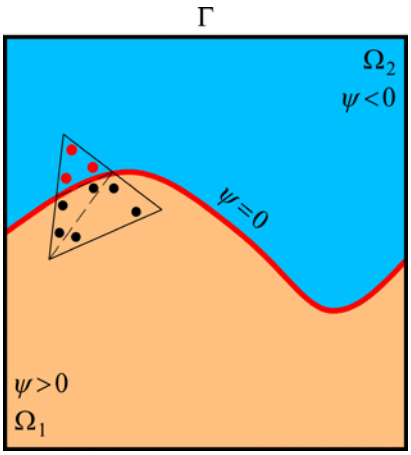

Figure 7. Modified integration rule for an element cut by the interface.

7 CONVERGENCE TEST FOR REGULARIZED BINGHAM'S MODELS

7.1 CONVERGENCE TEST

In this Section a convergence test is performed to compare the Papanastasiou model and the double-viscosity model proposed in Section 2.
The convergence test is carried out for a 2D Poiseuille flow for which the analytical is obtained in the next subsection. The numerical solution is obtained using different structured meshes of mixed Q1Q1 quadrilateral bilinear elements, stabilized with the split-OSS procedure.
For each of the computed cases, the error of the numerical velocity profile in the central section of the channel with respect to the analytical solution is calculated. The L_2-error for the velocity U is defined as

$$E = \frac{\left[\sum_{a=1}^{n_{node}} (U^a - u^a)^2\right]^{\frac{1}{2}}}{\left[\sum_{a=1}^{n_{node}} (u^a)^2\right]^{\frac{1}{2}}} \tag{7.1}$$

where n_{node} is the number of nodes in the central section of the channel, a is the considered node, U^a is the value of the velocity of the analytical solution and u^a is the corresponding numerical solution.

7.2 ANALITYCAL SOLUTION FOR IDEAL BINGHAM'S POISEIULLE FLOW

The analytical solution for Poiseuille flow is obtained for a 2D stationary flow between fixed infinite parallel plates. The procedure for obtaining this solution is analogous to that for Newtonian flows but contemplating the nonlinearity introduced by the Bingham fluid behaviour ([42], [43]).
The problem is depicted in Figure 8. The flow is produced by the pressure difference between the in-flow and the out-flow sections of the channel. The developed parallel flow is defined as $\mathbf{u} = (u_x, u_y)$, where $u_x = u(y)$ and $u_y = 0$. Zero velocity is imposed at $u(y = 0) = u(y = H) = 0$.
The Reynolds number is very small and inertial effects are neglected.

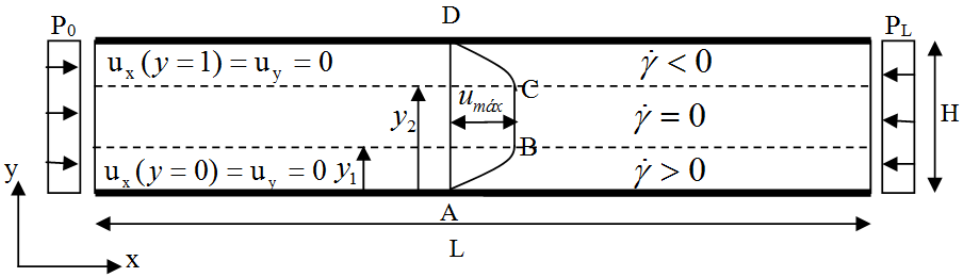

Figure 8. Poiseuille Flow. Geometry and boundary conditions.

The momentum equation for this flow reduces to

$$\frac{d\tau_{xy}}{dy} = \frac{dp}{dx} \tag{7.2}$$

with

$$\frac{dp}{dx} = -\Delta P = -\frac{P_0 - P_L}{L} \tag{7.3}$$

For a Bingham fluid with yield stress τ_y and plastic viscosity μ_0, the shear stress is:

$$\tau_{xy} = \mu_0\dot{\gamma} + \tau_y = \mu_0\frac{du}{dy} + \tau_y \tag{7.4}$$

In these conditions, three zones can be distinguished:

- Zone I, $0 \le y \le y_1$, where $\tau_{xy} > \tau_y > 0, \dot{\gamma} > 0$.
- Zone II, $y_1 \le y \le y_2$, where $\tau_{xy} = \tau_y, \dot{\gamma} = 0$.
- Zone III, $y_2 \le y \le H$, where $\tau_{xy} < -\tau_y < 0, \dot{\gamma} < 0$.

In Zones I and III the shear stress exceeds the yield stress, and the fluid flows; in Zone II, there is no shear rate, and the material moves rigidly. Ordinates y_1 and y_2 define the yielding surfaces as inter-zone limits. Note that the shear stress and the shear strain rate have corresponding signs, positive in Zone I and negative in Zone III.
It follows from Equations (7.2) and (7.3) that the shear stress is linear:

$$\tau_{xy} = -\Delta P y + c \tag{7.5}$$

where *c* is an integration constant. Equating Equations (7.4) and (7.5):

$$\mu_0\frac{du}{dy} + \tau_y = -\Delta P y + c \tag{7.6}$$

Equation (7.6) is integrated in the three zones imposing that:

- the velocity in the upper and bottom plate is zero, $u_x(y=0) = 0$, $u_x(y=H) = 0$
- the velocity and the strain rate are continuous at the ordinates y_1 and y_2.

The resulting velocity distribution is:

$$u_x = u(y) = \begin{cases} \frac{\Delta P}{2\mu_0}[y_1^2 - (y_1 - y)^2] & 0 \le y \le y_1 \\ \frac{\Delta P}{2\mu_0} y_1^2 & y_1 \le y \le y_2 \\ \frac{\Delta P}{2\mu_0}[(H - y_2)^2 - (y - y_2)^2] & y_2 \le y \le H \end{cases} \quad (7.7)$$

The positions of the yielding surfaces y_1 and y_2 are obtained from equating the shear stress ($\tau_{xy} = \tau_y$) and the velocities at those locations. From the first equation

$$y_2 - y_1 = \frac{2\tau_y}{\Delta P} \quad (7.8)$$

From the second

$$y_2 + y_1 = H \quad (7.9)$$

Therefore,

$$y_1 = \frac{H}{2} - \frac{\tau_y}{\Delta P}, \; y_2 = \frac{H}{2} + \frac{\tau_y}{\Delta P} \quad (7.10)$$

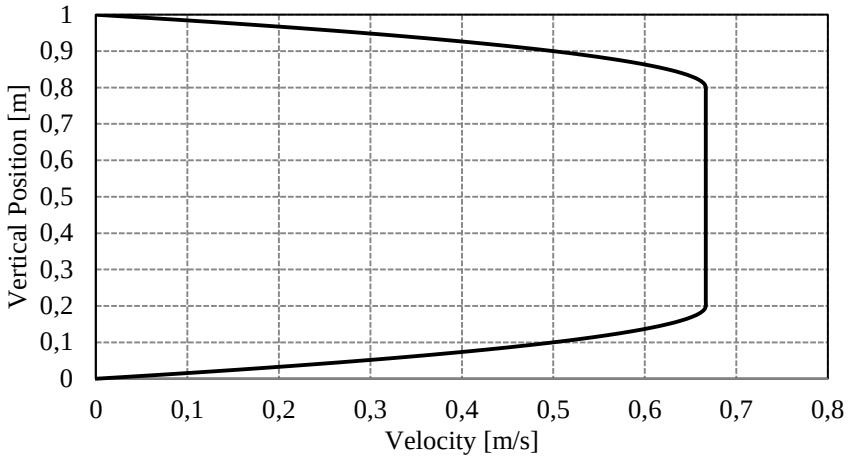

(a)

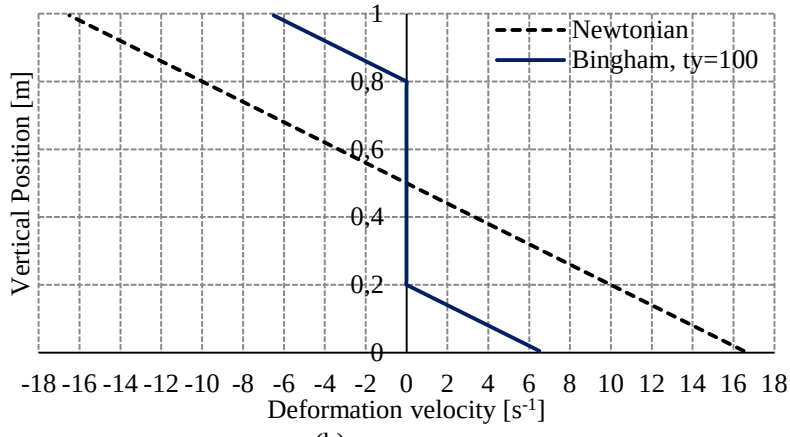

(b)

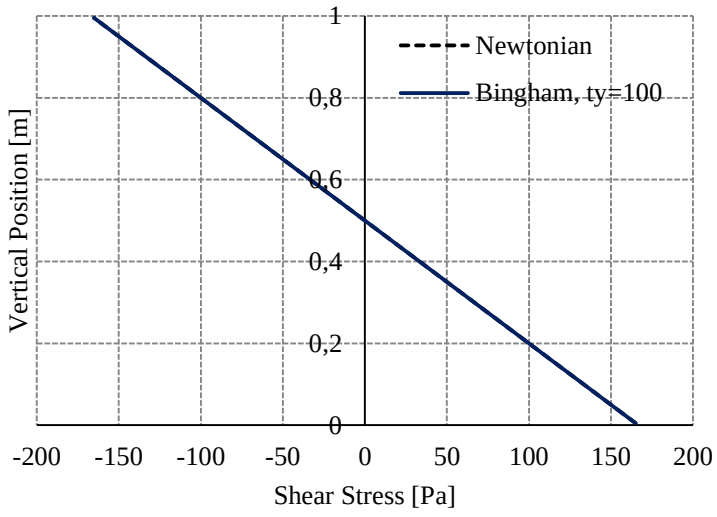

(c)

Figure 9. Poiseuille flow and ideal Bingham fluid:
a) velocity, b) strain rate, c) shear stress

The analytical solution for a channel section with H= 1 m, $\Delta P = 333.333$ Pa, $\tau_y = 100$ Pa and $\mu_0 = 10$ Pa.s is shown in Figure 9. The yielding surfaces are located at $y_1 = 0.20$ m and $y_2 = 0.80$ m. Comparison with a Newtonian fluid of the same viscosity is offered for the shear rate and stress. The velocity for the Newtonian case is parabolic with a maximum velocity of 4.166 m/s (not plotted).

7.3 ANALITYCAL SOLUTION FOR REGULARIZED BINGHAM'S POISEIULLE FLOW

7.3.1 REGULARIZED DOUBLE VISCOSITY BINGHAM FLUID

For the regularized double viscosity Bingham fluid, the procedure is very similar to the one for the ideal model. Recall that a regularization viscosity, $\mu_r = m\tau_y$, is defined in terms of the regularization time parameter m so that a critical deformation rate $\dot{\gamma}_c$ is defined as

$$\dot{\gamma}_c = \frac{\tau_y}{\mu_r - \mu_0} \tag{7.11}$$

and the critical stress τ_c corresponding to the critical viscosity is

$$\tau_c = \tau_y \frac{\mu_r}{\mu_r - \mu_0} > \tau_y \tag{7.12}$$

Now, three zones can be distinguished:

- Zone I, $0 \le y \le y_1$, where $\tau_{xy} > \tau_c > 0, \dot{\gamma} > \dot{\gamma}_c$.
- Zone II, $y_1 \le y \le y_2$, where $-\tau_c < \tau_{xy} < \tau_c, -\dot{\gamma}_c < \dot{\gamma} < \dot{\gamma}_c$.
- Zone III, $y_2 \le y \le H$, where $\tau_{xy} < -\tau_c < 0, -\dot{\gamma}_c < \dot{\gamma}$.

In Zones I and III the shear stress exceeds the critical stress, and the fluid flows; in Zone II, there is shear rate smaller than the critical. Ordinates y_1 and y_2 define the critical surfaces as inter-zone limits. Note that the shear stress and the shear strain rate have corresponding signs, positive in Zone I and negative in Zone III.

Following a procedure similar to one above, the resulting velocity distribution is:

$$u_x^{DV} = u_x + \begin{cases} \dfrac{\tau_c - \tau_y}{\mu_0} y & 0 < y < y_1 \\ \dfrac{\tau_c - \tau_y}{\mu_0} y_1 + \dfrac{\tau_c}{\mu_r}(y - y_1) - \dfrac{\Delta P}{2\mu_r}(y - y_1)^2 & y_1 \le y \le y_2 \\ \dfrac{\tau_c - \tau_y}{\mu_0}(H - y) & y_2 \le y \le H \end{cases} \qquad (7.13)$$

where u_x is the solution in (7.7) for the ideal fluid and the terms after the key are due to the regularization. All these terms vanish for $m \to \infty$. Note that the flow in the three zones is parabolic.

The positions of the critical surfaces y_1 and y_2 are

$$y_1 = \frac{H}{2} - \frac{\tau_c}{\Delta P}, \quad y_2 = \frac{H}{2} + \frac{\tau_c}{\Delta P} \qquad (7.14)$$

7.3.2 REGULARIZED PAPANASTASIOU BINGHAM FLUID

For the regularized Papanastasiou Bingham fluid, the differential equation for the velocity is

$$\left(\mu_0 \frac{du}{dy} + \tau_y\right)\left(1 - \exp\left(-m\frac{du}{dy}\right)\right) = -\Delta P y + c \qquad (7.15)$$

Figure 10 shows the distribution of the regularized effective viscosity across the thickness of the channel in the Poiseuille flow for the two regularized Bingham models, for $\tau_y = 100$ Pa, $\mu_0 = 10$ Pa.s and $m = 1000$. For such high regularization parameter, the velocity, shear strain rate and stress distributions for both regularized models overlap with those of the ideal model in Figure 9. This means that both models approximate the effective viscosity satisfactorily in the yielding zones; moreover, their corresponding regularizations are identical, as expected. Nevertheless, the difference between the models is neatly appreciated in the central zone of the flow. The DV-model shows a large constant viscosity $\mu_r = m\tau_y = 100{,}000$ Pa.s, while the Papanastasiou model shows a non-constant exponential trend with identical maximum value.

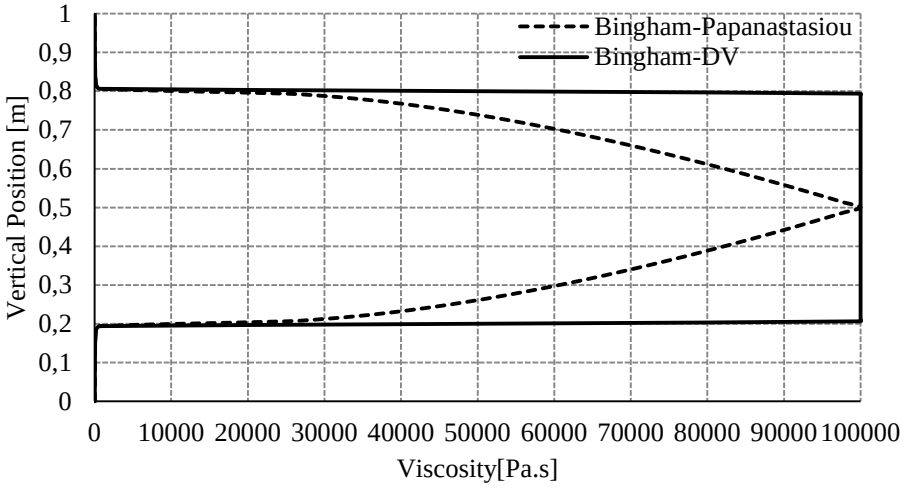

(a)

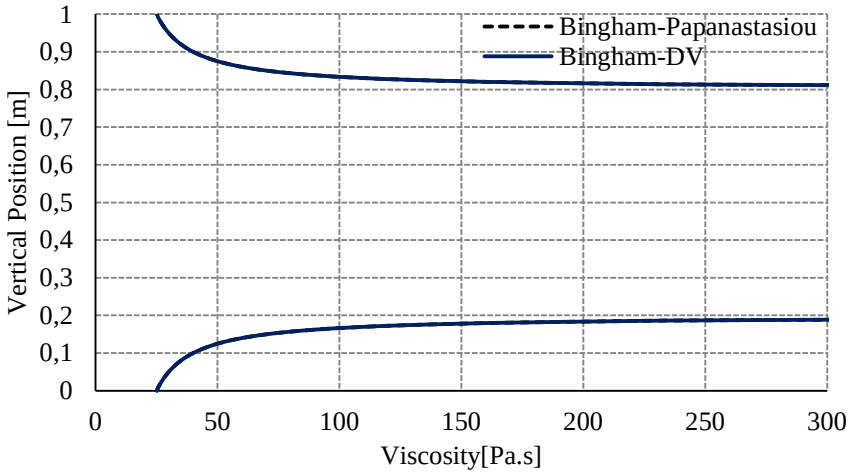

(b)

Figure 10. Poiseuille flow and regularized Bingham fluids:
a) effective viscosity, b) detail of effective viscosity

7.4 NUMERICAL SOLUTION FOR REGULARIZED BINGHAM'S POISEIULLE FLOW

The numerical solution of the Bingham - Poiseuille flow has been performed following the geometry depicted in Figure 8. A length L = 6 m is used.
The rectangular domain is discretised into a structured mesh of quadrilateral elements with 60 x 160 (H x L) elements.
The analytical solution for the ideal Bingham flow is compared to the solutions obtained with the Papanastasiou and DV regularized model, for increasing values of the regularization parameter. Figure 11 shows the corresponding L_2-error for the velocity. It can be seen that both models converge to the non-regularized solution with the same liner rate. Nevertheless, results obtained with the DV-model are closer to the exact solution at all instances. This can also be appreciated in Figure 2.

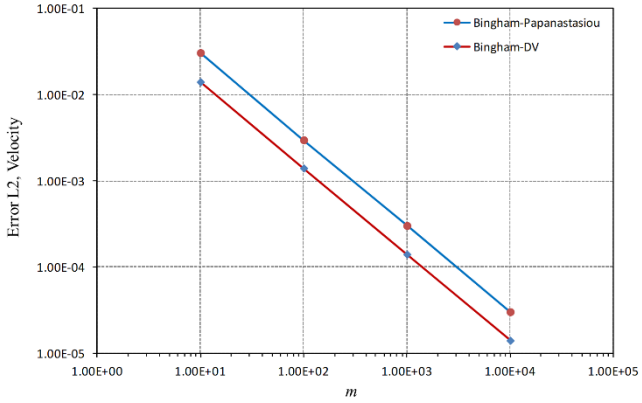

Figure 11. L_2-error for the velocity for the Papanastasiou and DV models.

Regarding the spatial resolution of the problem, the DV-Bingham model presents constant viscosity for all elements which are not intersected by the yielding surfaces. This feature translates in a better spatial approximation for the DV model, particularly when OSS stabilization is used. This is explained as follows.
For a constant viscosity Newtonian fluid, the analytical solution of the Poiseuille problem is a parabolic velocity field and the shear strain is linear. The discrete solution obtained using OSS stabilized linear elements on a structured regular mesh is exact at the nodes. This exactness is not achieved however using other stabilization procedures,

like the ASGS for instance.
For a Bingham fluid, the analytical solution of the Poiseuille problem is a piece-wise parabolic velocity field and the shear strain is piece-wise linear. Therefore, using OSS stabilized linear elements on a structured regular mesh and the regularized DV model yields the exact solutions at the nodes if the yield lines position coincides with a line of nodes; otherwise, the only numerical error associated to the discrete solution is the integration error of those elements intersected by the yield lines, whose viscosity is not constant. Using the regularized Papanastasiou model, whose viscosity depends continuously on the strain rate, the integration error occurs for all the elements in the domain.
Regarding the iterative procedure required by the Picard method to solve the nonlinear problem associated, precisely, to the nonlinearity of the viscosity and the location of the yielding surfaces, linear regularization is advantageous to the exponential regularization using OSS stabilized linear elements because of the above mentioned reason (see Figure 10a).

8 EXTRUSION FLOW WITH FREE SURFACE

8.1 DESCRIPTION OF THE PROBLEM

In this section, we study the problem of extrusion into the atmosphere of a viscoplastic fluid contained in a cavity through an exit orifice. This problem has been much more studied for a Newtonian fluid ([44], [45], [46]) than for a viscoplastic fluid ([47], [48]). The fundamental objective of the study is to determine the form adopted by the fluid domain outside the cavity. The free surface is the interface between the fluid domain and the air.
In this work, in a plane geometry, for Newtonian and Bingham fluids, the shape and location of the free surface once the fluid comes to the surface are found out. In the Bingham fluid the yielded and unyielded zones of the extruded flow are also determined.
The effect of surface tension is ignored. Stationary non-inertial flow (Stokes flow, yielded flow) is considered. The flow is parallel within the cavity; out of the cavity there is again a parallel flow, at a sufficient distance from the section of extrusion.
The dimensionless yield stress, τ_y^*, and the Bingham number, Bn, are

$$\tau_y^* = \frac{\tau_y H}{\mu V_n}, \qquad Bn = \frac{\tau_y 2H}{\mu V_B} \tag{8.1}$$

where H is half the width of the extrusion cavity, V_n is the average velocity of the corresponding Newtonian liquid with viscosity μ at the same pressure gradient, V_B is the average velocity of the Bingham fluid.
The dimensionless distance, x^*, and the positions, y^* and, y_{max}^* where the free surface is encountered are:

$$x^* = \frac{x}{H};\ y^* = \frac{h}{H};\ y_{max}^* = \frac{h_{max}}{H} \tag{8.2}$$

where x is the distance from the orifice exit, h is half the width of the extruded flow corresponding to the distance x and h_{max} is half the width of the extruded flow developed. H = 1 m is half the width of the entrance.

8.2 GEOMETRY AND BOUNDARY CONDITION

Figure 12 shows the geometry and boundary conditions for the problem of extruded flow to the atmosphere. Because of the symmetry of the problem, only the upper part of the domain is simulated.
The slip condition is imposed along the ABEF line. The fluid moves by the application of a pressure gradient. In the output section in B the pressure is zero. In the AC inlet a constant *P* pressure profile is applied in such a way that the desired pressure gradient is produced.
The velocity profile is fully developed in the inlet channel, which requires a minimum length of the inlet channel $L1$ (Figure 12).

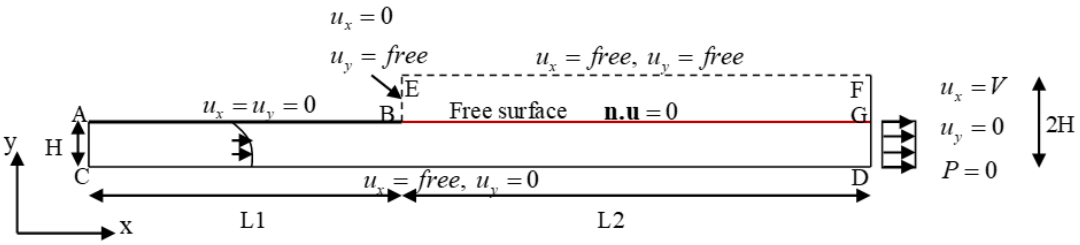

Figure 12. Extrusion flow. Geometry and boundary conditions

The length of the entrance channel is $L1$ = 10 m. For this value a completely developed solution for Bingham fluids is obtained. We have taken $L2$ = 15 m for which the velocity distribution at the GD outlet is completely horizontal and has a constant value, *V*. The slip condition is imposed along the plane of symmetry, CD.
The flow is produced by a pressure gradient defined as:

$$\Delta P = -\left(\frac{P_0 - P_L}{L1}\right) = -3\ Pa/m \qquad (8.3)$$

where P_0 is the pressure at the inlet of the cavity, P_L is zero pressure at the outlet and $L1$ is the length of the cavity.
The free surface is initially horizontal.

8.3 CONSTITUTIVE PROPERTIES AND REGULARIZATION PARAMETER

Table 1 shows the properties for the extrusion flow problem with the Bingham fluid.

Table 1. Constitutive properties and regularization parameter for extrusion flow.

Constitutive properties		
Fluid model	**Bingham fluid**	**Air**
Viscosity μ_0 [Pa.s]	1	1×10^{-6}
Yield stress τ_y [Pa]	0.1-2.9	-
Regularization		
Regularization parameter *m* [s]	1000	-

8.4 DISCRETIZATION

Table 2 shows the number of nodes and elements of the unstructured mesh M of triangular elements (P1-P1). It has been refined in the line where the free surface is initially located.

Table 2. Number of nodes and elements for unstructured mesh M for extrusion flow.

Unstructured	Number of nodes	Number of elements
M (h_{max}=0.05m)	20415	39603

8.5 NEWTONIAN FLUID

Figure 13 shows the maximum expansion ratio of the developed Newtonian flow, $\tau_y^* = 0$ or location of the free surface, y_{max}^*, once it comes to the atmosphere. It can be seen that it has an expansion ratio of 1.194 for $\tau_y^* = 0$. It corresponds to the maximum expansion ratio. This expansion ratio is similar to the numerical results obtained by Reddy and Tanner [49], Crochet and Keuning [50], Ellwood et al. [47] and Abdali and Mitsoulis [51]. For the Newtonian fluid, the position of the free surface is about 19% above its initial position according to data obtained experimentally by Goren and Wronski [52].

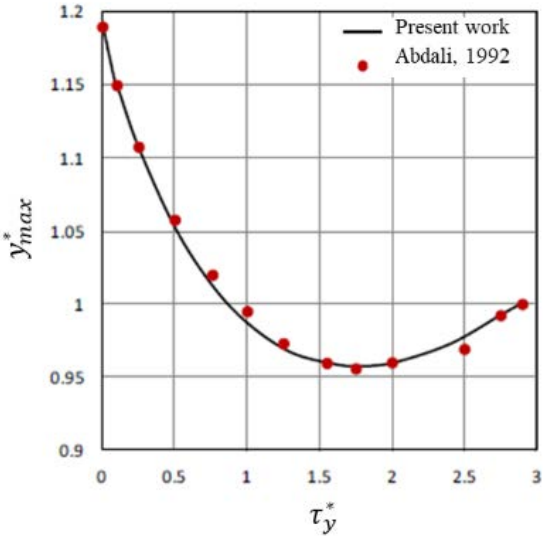

Figure 13. Extrusion flow. **Newtonian and Bingham fluid**. Maximum ratio of expansion for different dimensionless values of the yield stress.

8.5.1 VISCOPLASTIC BINGHAM FLUID

Figure 13 shows the maximum expansion ratio or location of the free surface, y_{max}^*, for the Bingham fluid with values of the dimensionless yield stress, τ_y^*, between 0.1 and 2.9. Once the fluid is extruded, the flow expands above $y_{max}^* = 1$ for dimensionless yield stress values less than $\tau_y^* \leq 0.88$. For larger values, the flow contracts to a minimum value of 0.957 in $\tau_y^* = 1.75$; and then, it begins to expand again until it reaches the value of $y_{max}^* = 1$ for $\tau_y^* = 2.9$. The results are in agreement with those obtained by Abdali and Mitsoulis [51].

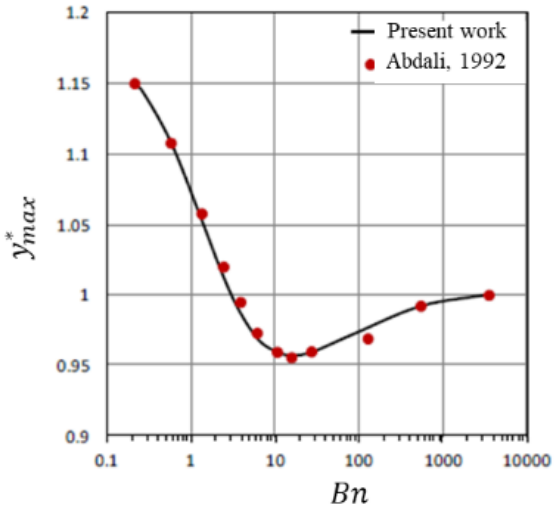

Figure 14. Extrusion flow. Variation of the cross section for different Bingham numbers.

Figure 14 shows the maximum expansion ratio or location of the free surface, y^*_{max}, for the Bingham fluid with Bingham numbers equivalent to the dimensionless yield stress of Figure 13. Once the fluid is extruded, the flow expands above $y^*_{max} = 1$ for Bingham number values less than $Bn \leq 3$. For larger values, the flow contracts to $Bn = 3519$ $\left(\tau^*_y = 2.9\right)$, presenting a minimum contraction value of 0.957 in $Bn = 15$ $\left(\tau^*_y = 1.75\right)$.

Figure 15 shows the position of the free surface given by the expansion ratio, y^*, for the Bingham fluid with dimensionless yield stress of $\tau^*_y = 1$ and $Bn = 0.21$ obtained in the present work compared with that of Ellwood. The free surface reaches a constant position at y^* =1.149 before and at a greater height than the result obtained by Ellwood of y^* =1.137 using the regularized Papanastasiou model. This is due to the use of the double viscosity model in the present work.

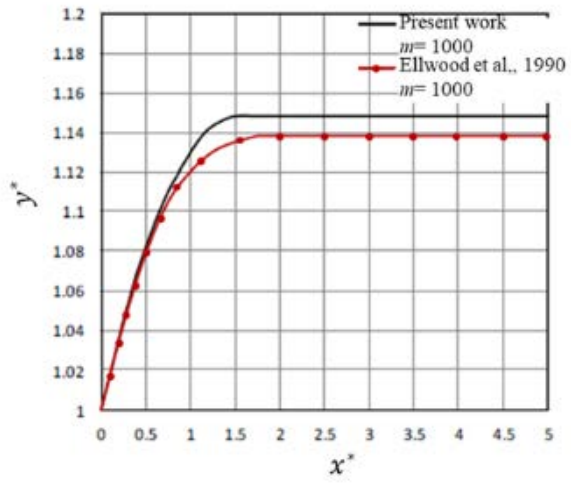

Figure 15. Extrusion flow. Profile of the free surface for a Bingham fluid with $\tau^*_y = 0.1$, $Bn = 0.21$

The results obtained for the free surface agree in a similar way with the results obtained by Abdali and Mitsoulis using the Papanastasiou regularized model for *m* = 200 s [51]. The position of the free surface obtained for different dimensionless values of yield stress and Bingham numbers from the Newtonian fluid is shown in Figure 16. It can be seen how the free surface shows the expanded flux for the dimensionless yield stresses of $\tau_y^* = 0, 0.25, 0.5$; for values of $\tau_y^* = 1.6, 2$, the flow contracts and for $\tau_y^* = 2.9$ $(Bn = 3519)$ the flow is practically parallel $(y_{max}^* = 1)$. For $\tau_y^* = 2.75$ the extruded material behaves as quasi-rigid.

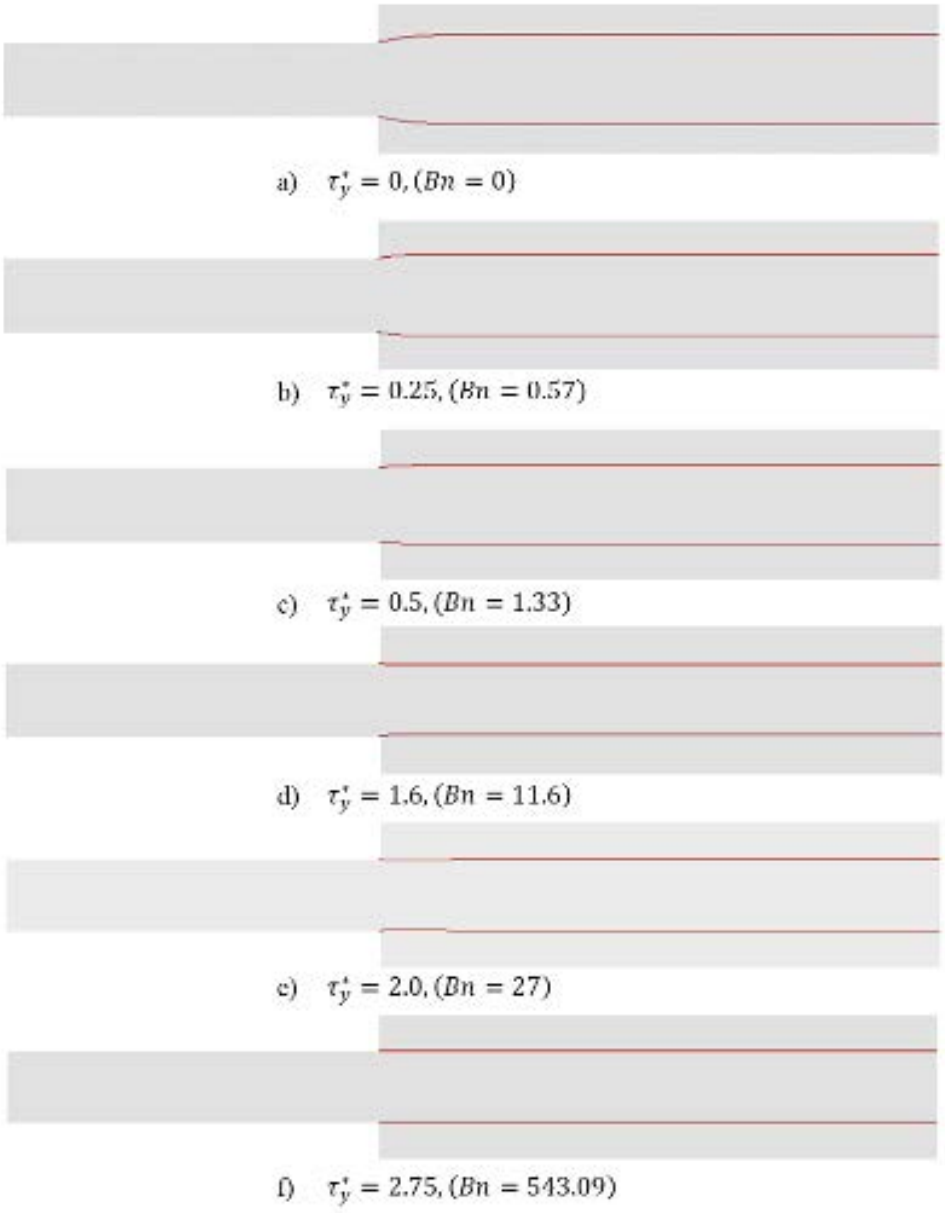

Figure 16. Extrusion flow. **Newtonian and Bingham fluids**.
Free surface for the extruded fluid for different values of yield stress.

The free surface and the yielded and unyielded zones for different Bingham numbers are presented in Figure 17. The zones of yielded (grey) and unyielded (color) of the extruded flow are delimited by the free surface, outside of this, the material is air. The yielded zones decrease as the number of Bingham increases until they turn completely to unyielded zones approximately from $\tau_y^* = 2.75$. As the number of Bingham

increases, the behavior is less fluid, becoming almost completely rigid for $\tau_y^* = 2.75$. The results are very similar to those found by Abdali and Mitsoulis.

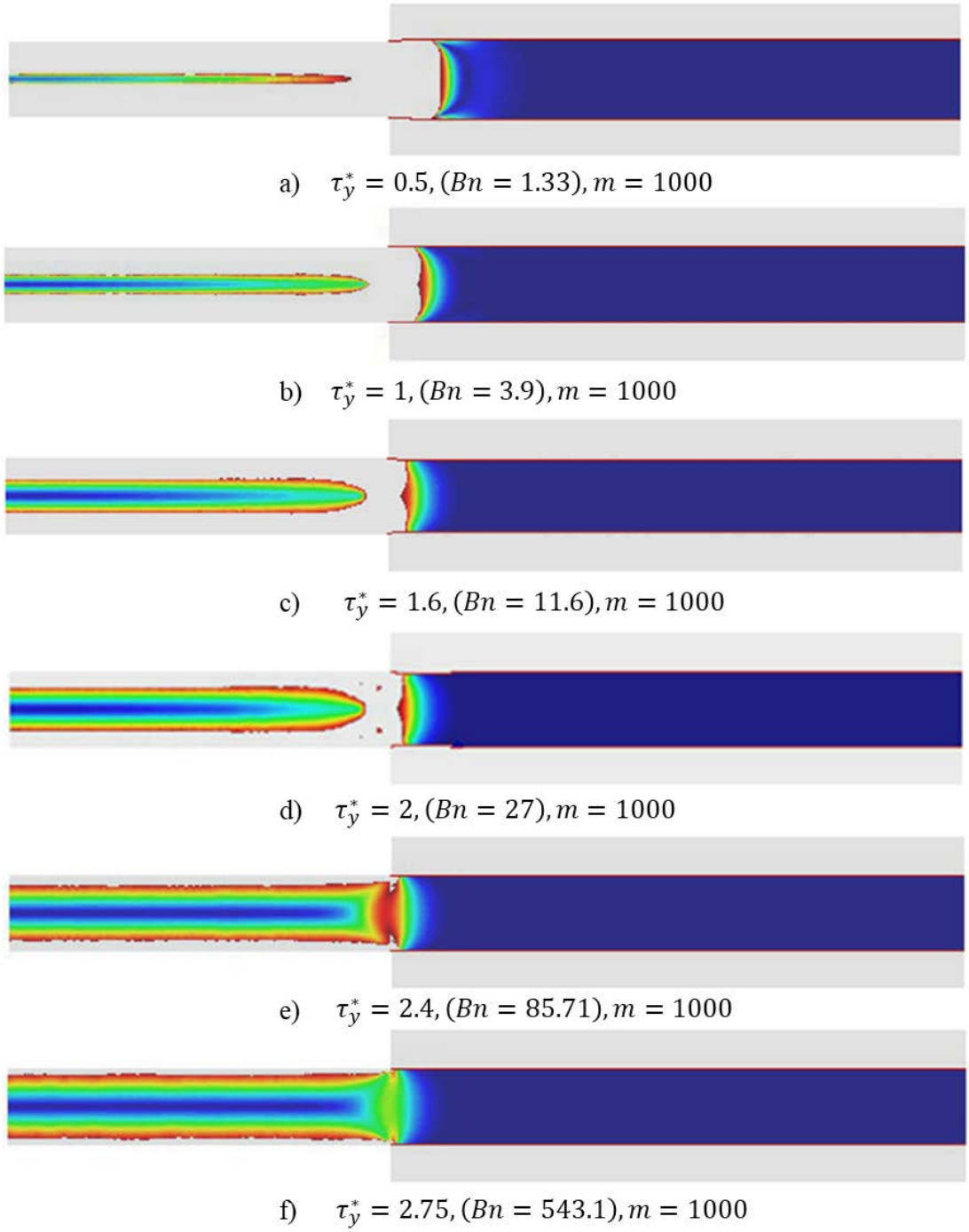

Figure 17. Extrusion flow. Progressive growth of unyielded zones in the extruded fluid.

Figure 18 shows the free surface and the yielded and unyielded areas for *Bn* = 27 and values of the regularization parameter *m* = 200, 1000. The difference that can be observed is in the islands in unyielded zone near the outlet to the atmosphere. For *m* = 1000 the islands almost disappear. For *m* = 200 these islands are larger, as expected. On the other hand, for *m* = 200 these islands are a little smaller than those found by Abdali and Mitsoulis with the regularized model of Papanastasiou. This shows that the double

viscosity model approximates better the ideal Bingham model than the standardized Papanastasiou model.

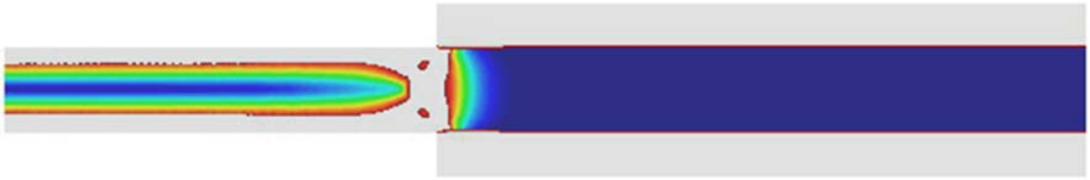

a) $\tau_y^* = 2, (Bn = 27), m = 200$

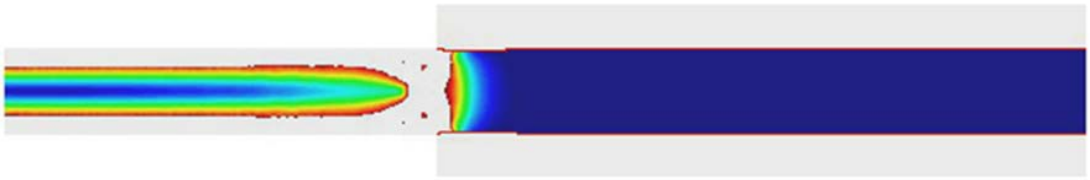

b) $\tau_y^* = 2, (Bn = 27), m = 1000$

Figure 18. Extrusion flow. Variation of the yielded and unyielded zones of the extruded fluid for *Bn* = 27 and different values of *m*.

9 WATER AND OIL SPILLAGE DUE TO DAM-BREAK

9.1 DESCRIPTION OF THE PROBLEM

The problem of the flow due to the dam-break consists in Newtonian or non-Newtonian fluids moving on the Earth surface once a dam breaks.

The prediction of the real behavior of these flows is extremely difficult due to the different factors involved, such as the geology of the area, the topography, the climatic factors, as well as the physical and mechanical properties that interrelate with each other within the rheology of the material.

In this work, the mathematical and numerical model is formulated using the Navier-Stokes equations. The free surface is found by the level set method in the same way as in the extrusion flow problem. Inertial effects are considered and the flow is transitory.

In particular, in this section the problem of the Newtonian flow of water and oil due to dam breakage is evaluated. The numerical solution is similar to the one used in the extrusion flow problem. The results obtained from the free surface, height of water or oil surface and the location of the flow front, also called flood distance, for the water flow is compared with the Chanson analytical solutions [9] and the Schoklitsch experiment [53]. Likewise, the results obtained for the oil flow are compared with the Jeyapalan experiments [54] for a horizontal channel and an inclined channel.

The distance of the flow front and the height of the water surface are dimensionless, x^* and h^*, as:

$$x^* = \frac{x}{\sqrt{\frac{g}{h_0}t}};\ h^* = \frac{h}{h_0} \tag{9.1}$$

where *x* is the horizontal distance from the location of the dam, *h* is the height of the fluid surface corresponding to the distance *x*, *g* is the acceleration of gravity and *t* is the time instant, measured from the break of the dam.

9.2 GEOMETRY AND BOUNDARY CONDITION

Figure 19 shows the geometry and boundary conditions for the water flow problem. It is a horizontal channel. The initial height of the water surface is h_0 = 0.074 m, height of the dam (or gate). The initial position of the free surface (red line) representing the water reservoir is known. The friction at the bottom of the channel is simulated by a wall law [55]. The right side is with free velocity; in the rest of the contours, a free slip condition is imposed. In the corner that intercepts the left side with the bottom of the channel, the velocity is set to zero.

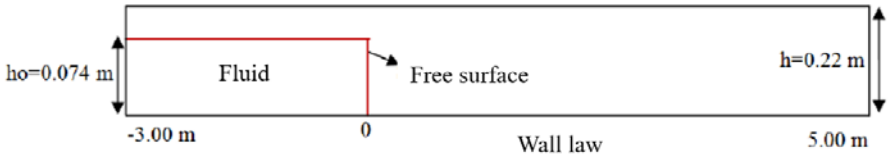

Figure 19. Dam-break. Geometry and boundary conditions for water flow

Figure 20 shows the geometry and boundary conditions for the oil flow problem. The initial height of oil surface for the horizontal channel is h_0 = 0.1526 m and for the channel with slope of 4° is h_0 = 0.2286 m. The initial position of the free surface (red line) matches the oil reservoir. The boundary conditions are used for both the horizontal channel and the channel with a 4º slope. The friction at the bottom of the channel is also modelled by a wall law. The right side has free velocity, in the rest of the boundary, a free slip condition is imposed. In the corner that intercepts the left side with the bottom of the channel, the velocity is set to zero.

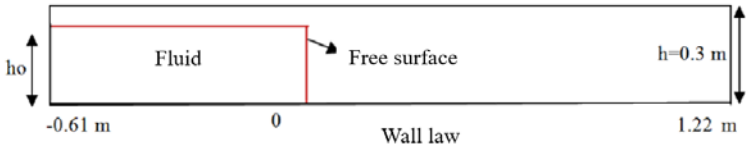

Figure 20. Dam-break. Geometry and boundary conditions for oil flow. Configuration for the horizontal and sloping channel

9.3 CONSTITUTIVE PROPERTIES

Table 3 shows the constitutive properties used in the problem of water and oil flows due to dam breakage.

Table 3. Constitutive properties for water and oil flow due to dam-break.

	Constitutive properties		
Fluid model (Newtonian)	Water	Oil	Air
Viscosity μ_0 [Pa.s]	1×10^{-3}	3.9	1×10^{-6}
Density ρ [kg/m^3]	1000	896	1.2

9.4 DISCRETIZATION

The mesh M1 is used for the water flow. In case of the oil flow, the meshes M2 and M3 are adopted for the horizontal and inclined channels, respectively. These meshes are unstructured and formed by triangular elements (P1-P1). Table 4 shows the number of corresponding nodes and elements.
Based on the mesh size and the expected flow velocities a time step of 10^{-2} s is used.

Table 4. Number of nodes and elements for different meshes for dam-break.

Unstructured	Number of nodes	Number of elements
M1 (h_{min}=0.004 m)	59670	116468
M2 (h_{max}=0.01 m)	3393	6412
M3 (h_{max}=0.01 m)	19820	36906

9.5 FREE SURFACE AND DISPLACEMENT OF THE FLOW FRONT

Figure 21 shows the displacement of the fluid on the bottom of the channel and the free surface at time t = 3.75 s. It can be seen that the height of water decreases as the fluid moves. The flow front has a rounded shape.

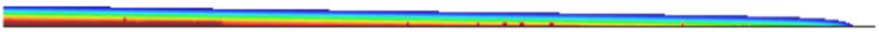

Figure 21. Water flow due to dam-break. Free surface and water height at t = 3.75 s

Figure 22 shows the results for the dimensionless height of the water of the experimental data of Schoklitsch [53] at dimensionless time of 43; of the analytical solution of Chanson [9] for a time of 3.75 s and coefficient of friction f = 0.03 [9]; of the Ritter solution [5] for an ideal fluid and of the present work at time t = 3.75 s. Here, the height of the water surface has decreased approximately half of its initial height. The flow front has a rounded shape, defined by the free surface, and starts approximately from the dimensionless length of 0.4. The free surface behind the flow front fits with the ideal Ritter fluid.

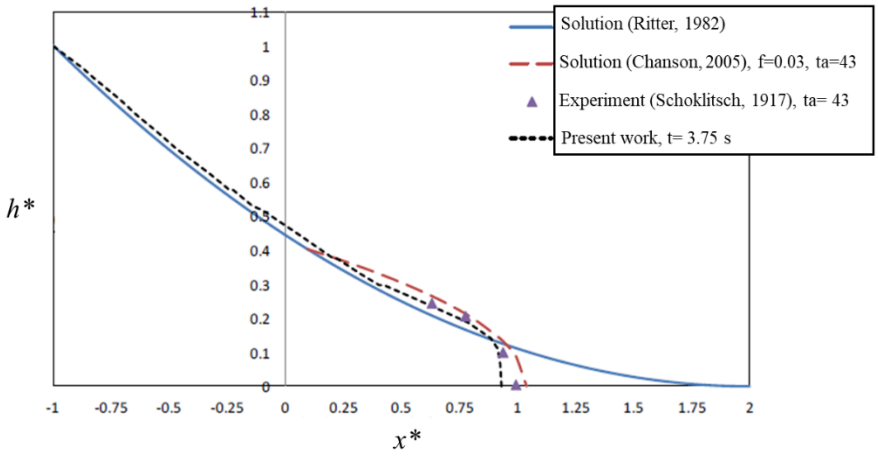

Figure 22. Water flow due to dam-break.

Comparison of the location of the free surface with the experimental data and analytical solutions at t = 3.75 s.

The results obtained for the dimensionless height of the water surface fit well with the Schoklitsch experimental results of the flow front [53], and agree with the results shown by Chanson for a bottom with smooth roughness.
Figure 23 shows the free surface of the oil flow due to the dam-break in the horizontal channel at different times. It can be seen that the fluid moves downstream due to gravity as a consequence of the dam-break. At the first moments, t = 2, 2.75 s, the flow moves much faster than for the next steps t = 3, 4 s; at t = 6 s the flow practically stops.

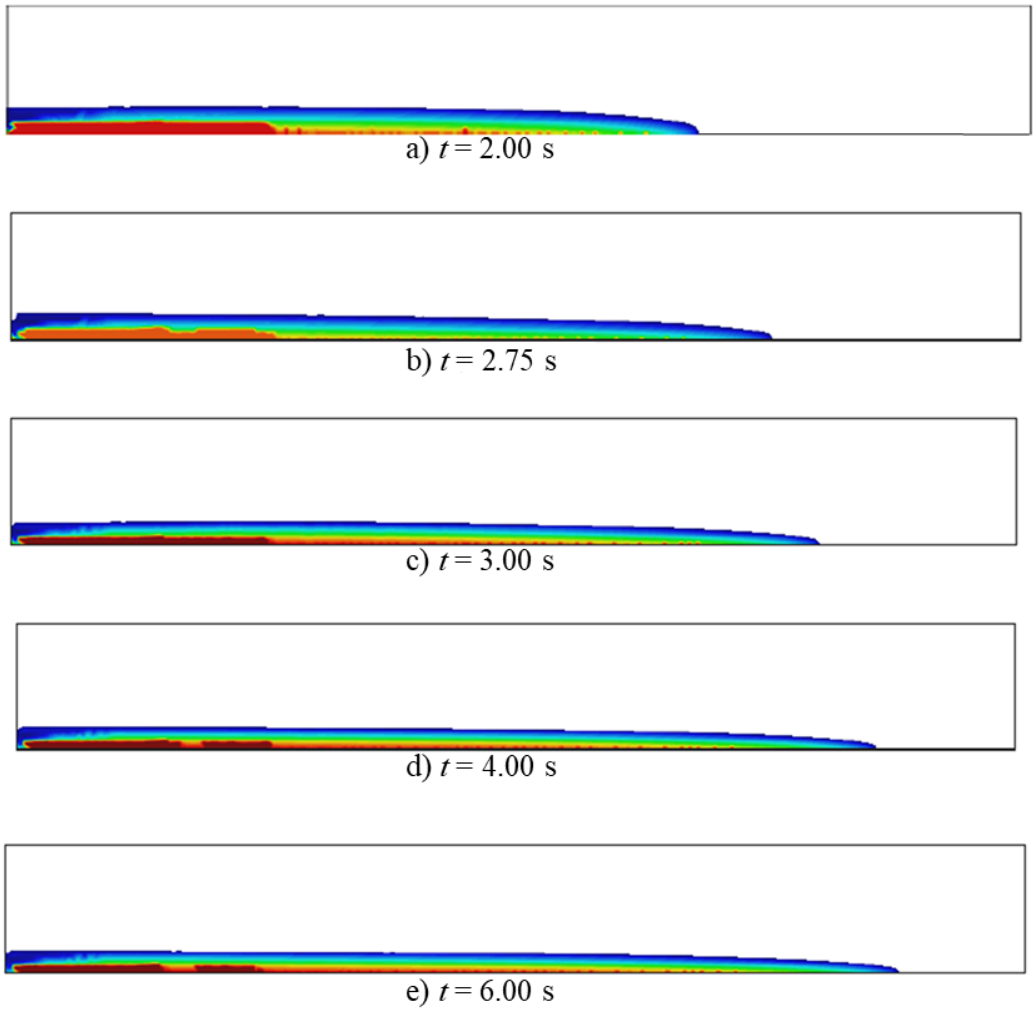

Figure 23. Oil flow due to dam-break. Free surface of the oil flow in the horizontal channel for different instants of time.

Figure 24 shows the free surface of the oil flow due to the dam-break in the inclined channel at different instants of time. It is also observed that for the first instants of time, t = 2, 2.75 s, the flow moves much faster than for the following steps t = 3, 4, 4.96 s; at t = 4.96 s the flow reaches the right side of the channel. The slope contributes to the increase of the flow velocity; therefore, the flow front reaches greater displacement in the sloping channel than in the horizontal channel.

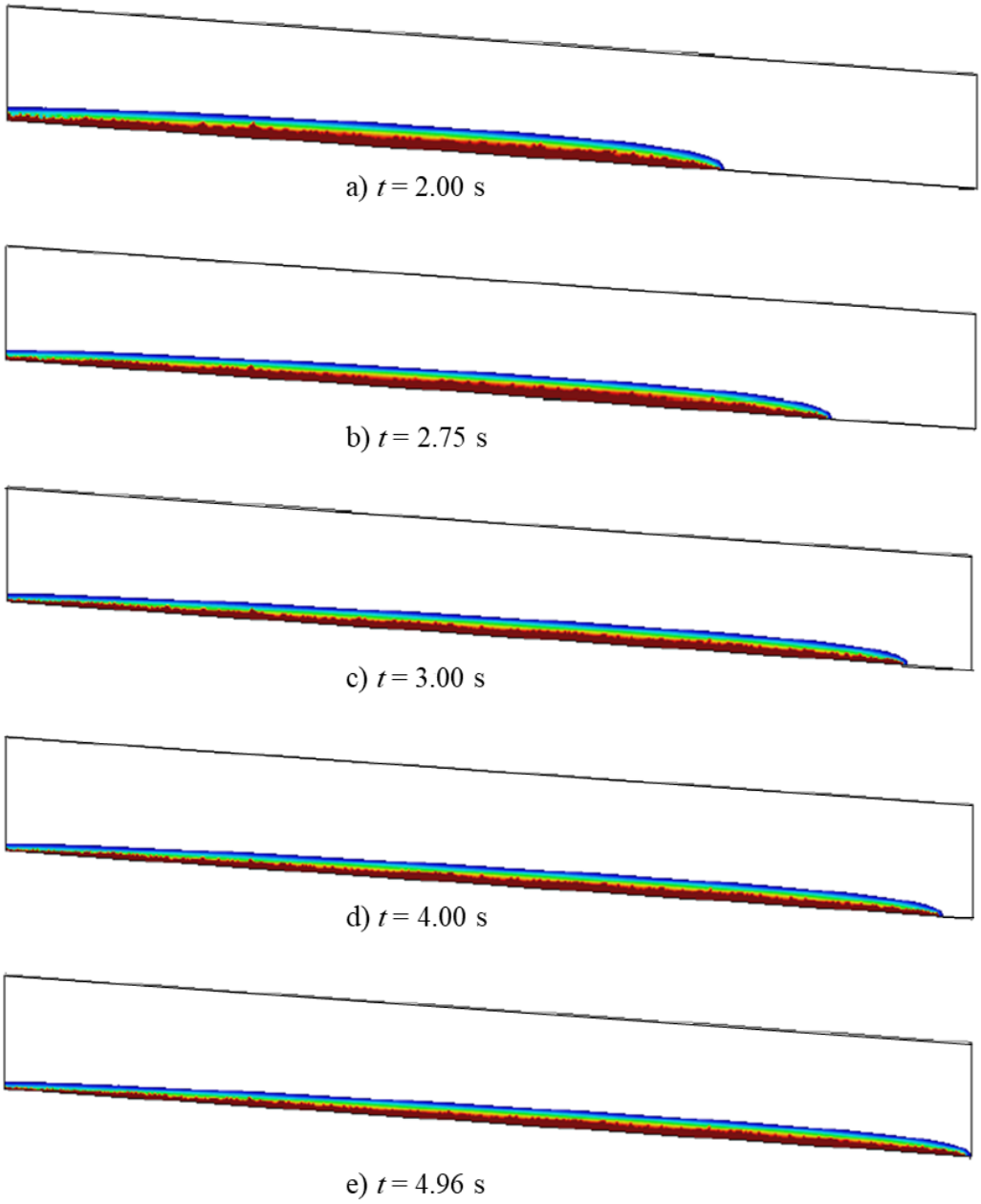

Figure 24. Oil flow due to dam-break. Free surface of the oil flow in the inclined channel for different instants of time.

Figure 25 shows the displacement of the flow front from the location of the dam in horizontal and sloping channels at different times. It is noted that the flow front in the sloping channel advances faster than the flow in the horizontal channel. The numerical results of the flow front distance at different time matches well with the experimental results of Jeyapalan et al. [54] for the horizontal channel (Figure 25a)) and for the sloping channel (Figure 25b).

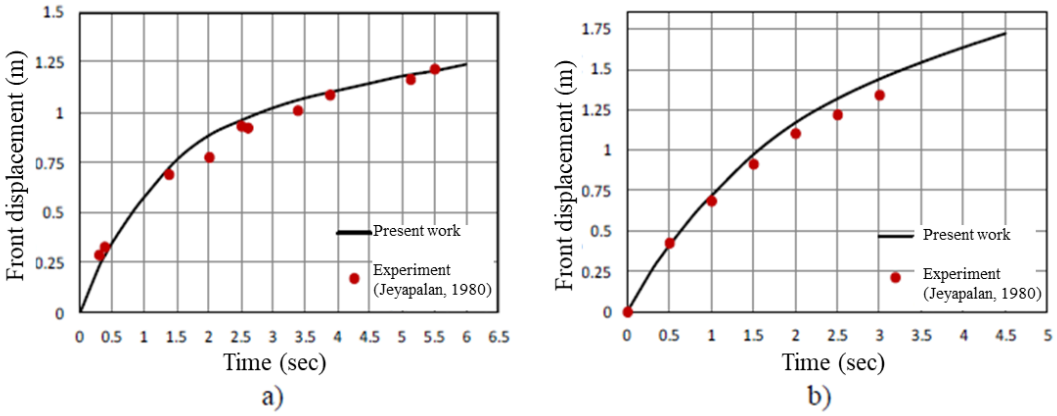

Figure 25. Oil flow due to dam-break. Comparison of the numerical results of the distance of the flow front with the experimental evidence for different instants of time. a) Horizontal channel. b) Inclined channel.

10 CASE STUDY OF A BINGHAM FLOW DUE TO THE RUPTURE OF A MINING TAILINGS DAM.

10.1 DESCRIPTION OF THE PROBLEM

The flows due to dam-break may also involve non-Newtonian fluids formed by a mixture of solid material from geological, industrial or mining material and inter-granular fluid [56]. These are the so-called debris flows. The viscoplastic models of Bingham fit a large part of these materials, especially in slurries and semi-granular materials.

In this section, we study the failure of the dam in East Texas, United States, in 1966, whose storage is made up of plaster waste. The dam failed as a consequence of interstitial pressures at the foot of the slope. A 3D numerical analyses are carried out in this case study in order to determine the free surface of the released material as it moves on the ground and the flow front distances at different time. The stoppage time of the flow and the average speed of the flow is also determined. The results are compared with field data of the event. A 2D simulation of the problem along a chosen longitudinal section is also performed to allow comparison with other analyses 2D analyses in the literature.

10.2 GEOMETRY AND BOUNDARY CONDITIONS

The mining tailings dam located in eastern Texas, United States, had a rectangular ground plan. Once the dam broke, the flows moved downstream at distance of 300 m according to field observations. Figure 26 shows the analysis domain for the three-dimensional flow problem with a total height of h = 16 m, the reservoir facility and the area where the waste moved. The reservoir is located on the left side. The distance D = 140 m corresponds to the breaking width of the dam [57].

The bottom of the domain has a length of D = 600 m, the initial longitudinal distance of the material storage is D = 200 m and the longitudinal distance to determine the displacement of the flow in the numerical analysis is D = 400 m. The dam front is located at x = 0 m.

Figure 27 shows the initial position of the free surface in the three-dimensional analysis, which coincides with the surface of the mining waste before the flow of these materials.

The initial height of the waste is h_0 = 11 m, height of the dam; the present simulation initiates with the fluid flow at the dam front, at x = 0 m. At the bottom of the domain a non-slip condition is imposed, the roof and sides shown in figure 27 have natural conditions. Zero velocity is assigned to the nodes at the bottom of the storage.

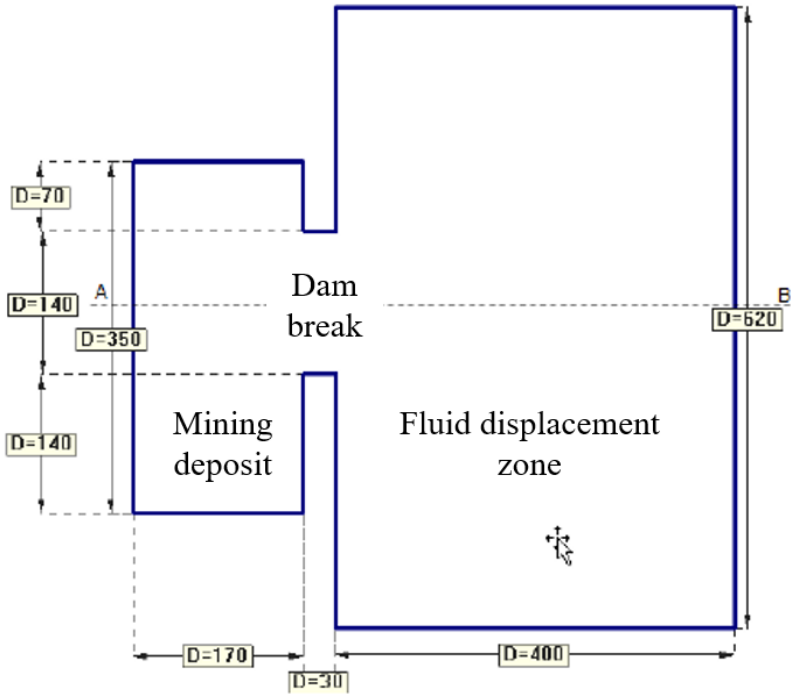

Figure 26. Mining tailings dam. Geometry in the reservoir facility and domain downstream of the dam.

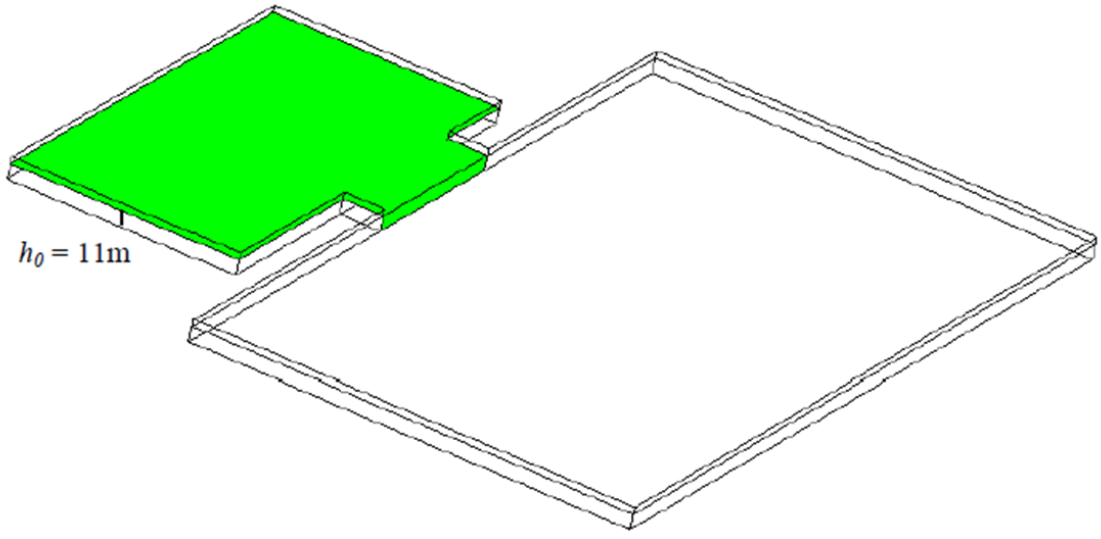

Figure 27. Mining tailings dam. Initial location of the free surface for the 3D case.

In order to allow comparison with analytical and numerical simulation reported in the literature, a longitudinal section AB is taken in the center of the three-dimensional domain of the dam-break, see figure 26. The flow is studied as a viscoplastic Bingham

fluid that initially is at rest and when the instantaneous dam breakage occurs, it moves along the domain due to gravity.
Figure 28 shows the geometry and boundary conditions, section AB, used in the 2D numerical analysis. It is a horizontal domain. The free surface (red line) coincides with the waste reservoir. The initial height of the mining waste is h_0 = 11 m, height of the dam.
On the right side and on the upper side no conditions are imposed (outlet x = 400 m); in the rest of the boundaries, a free slip condition is imposed. The corner that intercepts the right side with the bottom of the domain and the upper side is with natural conditions. In the rest of the corners, zero velocity is imposed. At the boundary, a non-slip condition is imposed.

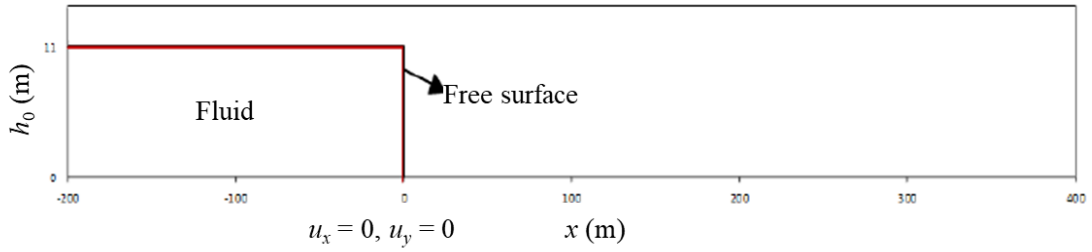

Figure 28. Mining tailings dam. Geometry and boundary conditions.

10.3 CONSTITUTIVE PROPERTIES AND REGULARIZATION PARAMETER

The material involved in the flow has the characteristics of a non-plastic silt, with a particle diameter of $D_{50} \approx 0.07$mm, a uniformity coefficient of around 3, the density of the particles around 2450 kg/m^3 and an average water content w of around 30% [46]. Density of 1400 kg/m^3 and an approximate yield stress of 1000 Pa (determined with a slope stability analysis) are considered. By correlation between the plastic viscosity of the material and the water content, a material plastic viscosity $\mu_0 = 1.500\left(\frac{90}{w}\right)^{3.2} = 50.44$ Pa is obtained [54]. A The value of 48 Pa has been used in order to compare with the results obtained by Herreros [57] for this problem.
Table 5 shows the constitutive properties and the regularization parameter used in the dam breakage problem for the 2D and 3D cases.

Table 5. Constitutive properties and regularization parameter for the flow of plaster waste due to breakage of the dam, Texas, United States.

Constitutive properties		
Fluid model	Bingham-DV	Air
Viscosity μ_0 [Pa.s]	48	1×10^{-6}
Density ρ [kg/m^3]	1400	1.2
Yield stress τ_y [Pa]	1000	-
Regularization		
Regularization parameter m [s]	1000	-

10.4 DISCRETIZATION

The M1 mesh used in the 3D case with P1-P1 tetrahedral elements has 1.54 million nodes and 8.69 million elements (see Figure 29). M2 mesh is used for the 2D case of P1-P1triangular elements. Table 6 shows the number of nodes and elements for unstructured meshes M1 and M2. Both meshes are refined at the bottom of the domain. Based on the mesh size and the expected flow velocities a time step of 10^{-1} s is used.

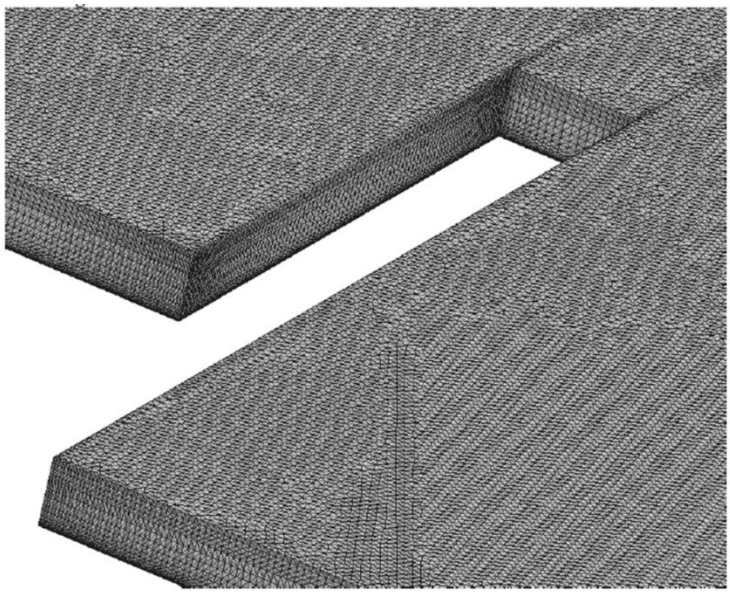

Figure 29. Mining tailings dam. Detail of the unstructured mesh M1.

Table 6. Number of nodes and elements for unstructured meshes M1 and M2.

Unstructured	Number of nodes	Number of elements
Mesh M1	1543680	8690163
Mesh M2	78536	149480

10.5 3D SIMULATION

Figure 30 shows the evolution of the free surface at different times, t = 0, 8, 30, 60, 62 s. Distance is measured from the dam front. In Figure 30a, t = 0 s, the flow is at its initial state of rest. Once released, the material in the front and the material on the surface upstream of the dam, the fluid passes from the unyielded condition to the yield condition, the stress exceeds the yield stress and it begins to move. The material in motion is directed downstream of the dam. At t = 8 s the flow front moves along the part of the domain that was initially dry. The free surface of the flow has a smooth profile and steep slopes. In Figure 30c, t = 30 s, the flow front has surpassed half of the maximum displacement. The movement is faster in the first moments of time. In Figure 30d, t = 60 s, the front has reached most of the maximum displacement, and the speed is lower. The movement becomes very slow and the material stops at t = 62 s, Figure 30d. The gravity force fails to overcome the yield stress of the fluid. The flow has reached a maximum displacement or flood distance of x_f = 255.40 m from the dam front, with a maximum height h_0 = 8.257 m on the left side of the discharge domain. This indicates that the free surface is located below its initial position and all the surface material in the 170 m long reservoir is mobilized, to reach a flood distance of 285 m from the mining deposit. In the field observations, the surface fluid mobilized in the reservoir reached 110 m and the distance of the flow front reached 300 m from the deposit.

The three-dimensional evolution of the flow at different times in isometric and plane views is shown in Figures 31 and 32, respectively. The actual geometry of the problem and the shape of the upstream storage defines the manner in which the material moves. It can be observed that at t = 8 s the material in the storage has not been completely mobilized and at t = 30 s, in the lower left corner of the storage, the surface material is at rest. These areas in the storage are best identified in Figure 32a and b with the light blue color. Also, lateral displacement and spreading of the material play a significant role. The flooded area (downstream of the broken dam) is approximately symmetric with respect to section AB.

10.6 2D SIMULATION AND COMPARISON

In the simplified 2D simulation the overall trend is very similar to the more realistic 3D case. The flow reaches a flood distance of x_f = 318 m and a maximum height h_0 = 6.718 m on the left side of the discharge domain.
Figure 33 compares the evolution of the free surface in the 3D and 2D simulations. Distance is measured from the dam front. The effect of the geometry of the upstream storage and the lateral movement and spreading of the material downstream are completely absent from the 2D simulation and this causes somewhat dissimilar profiles of the free surface.
Table 7 compares the numerical results with the field data, and the numerical results obtained by Herreros [57] and the analytical and the results of the TFLOW program obtained by Jeyapalan et al. [54]. Herreros [57] used a model integrated in the depth, where the vertical velocity is ignored, and a frictional fluid with a dissipation mechanism of interstitial pressures. The analytical model in [54] assumes an infinite impoundment volume while the corresponding numerical model does not.
The results of the present 3D and 2D simulations correlate well with the field data of the real event; stoppage time and average velocity are within the observed range, with the reported flood distance in between those calculated here.

Table 7. Mining tailings dam. Comparison of the results of the present work with observations in the field, analytical and numerical results.

	Observed values	Present work 3D	Present work 2D	Numerical results 3D [57]	Analytical results 2D [54]	Numerical results 2D [54]
Flood distance (m)	**300**	**285**	**348**	310	550	470
Stoppage time (s)	**60-120**	**62**	**87**	105	132	85
Average velocity (m/s)	**2.5-5.0**	**4.1**	**3.7**	3.0	4.2	5.5

11 SUMMARY AND CONCLUSIONS

In this work, numerical solutions have been presented for Newtonian and Bingham viscoplastic flows with a free surface. Extrusion flow with free surface and flow due to dam-Break resulting in spillage and debris floods have been investigated. The first has been studied as a non-inertial flow and the second as a transient flow.

The Bingham-DV double viscosity model and the split-OSS stabilization method have been used. In the solution of flows with free surface the Eulerian formulation in a fixed mesh has been used. This formulation has solved the problem by uncoupling the fluid domain from the air. For the location of the free surface, the level set method has been used.

A convergence test has been performed on the regularized Bingham models applied to the solution of a Poiseuille flow for which the analytical solution is obtained. The DV model shows better approximation properties both to the ideal model and with respect to the spatial discretization.

In the solution of the problem of extrusion flow with free surface, the yielded and unyielded zones for different Bingham numbers have been adequately obtained. As the Bingham number increases, the size of the unyielded zones increases.

The flow due to dam-break has been simulated in 2D and 3D. In the solution of the flow due to dam-break, the position of the free surface, the height of the fluid sheet at any point along the flow path and the flood distance have been obtained for the Bingham flow. In the Newtonian case the solution is shown to agree with the analytical solution of Ritter, Chanson and Schoklitsch.

The real event of the failure of the mining tailings dam in Texas has been simulated. The ensuing debris flow of mining waste is reproduced in actual 3D geometry and in a simplified 2D model. The results obtained are compared to the analytical, numerical solutions and to the field data available. The 3D solution agrees well with field observations.

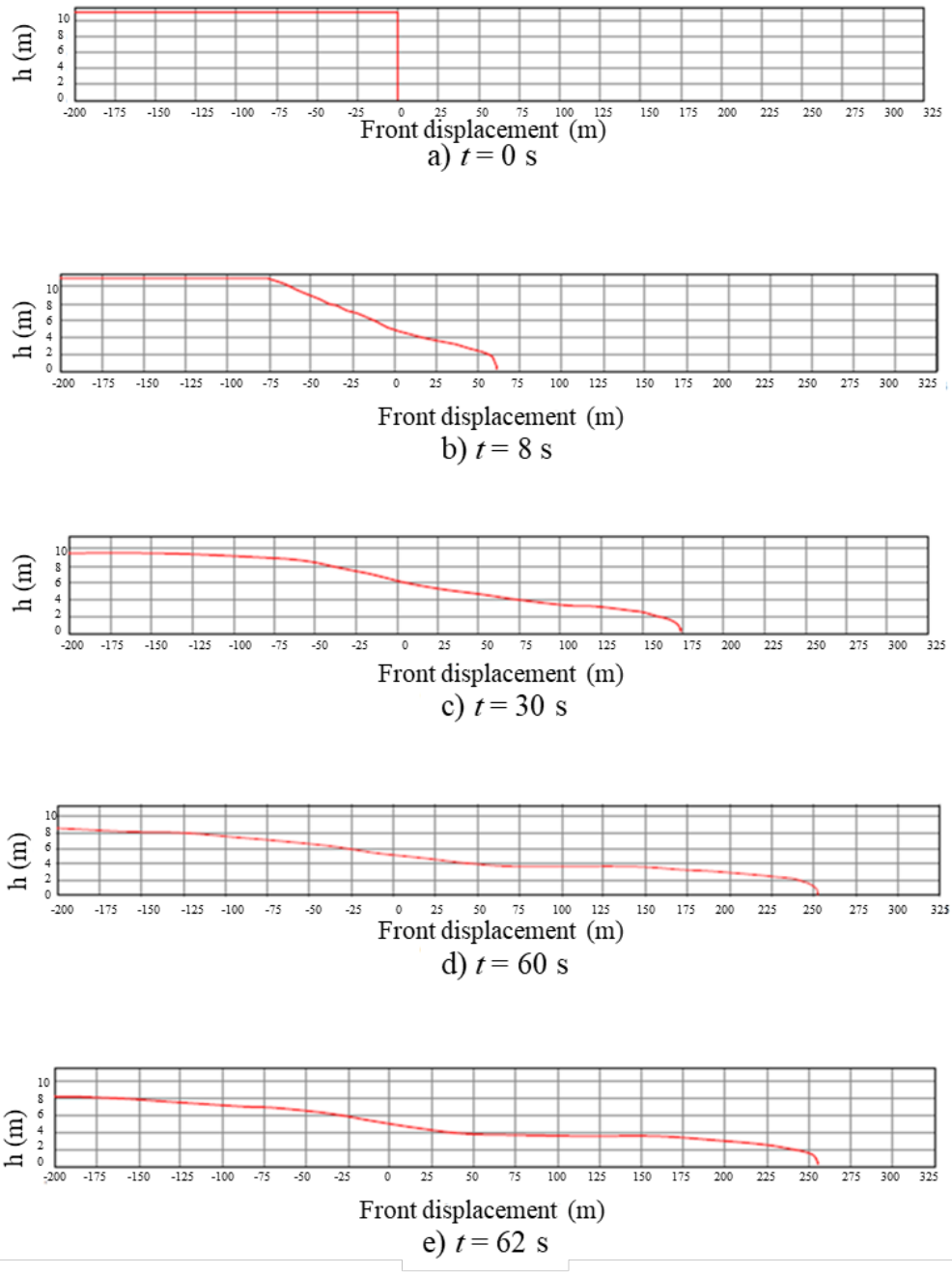

Figure 30. Mining tailings dam. 3D simulation. Evolution of the free surface in the fluid displacement zone.

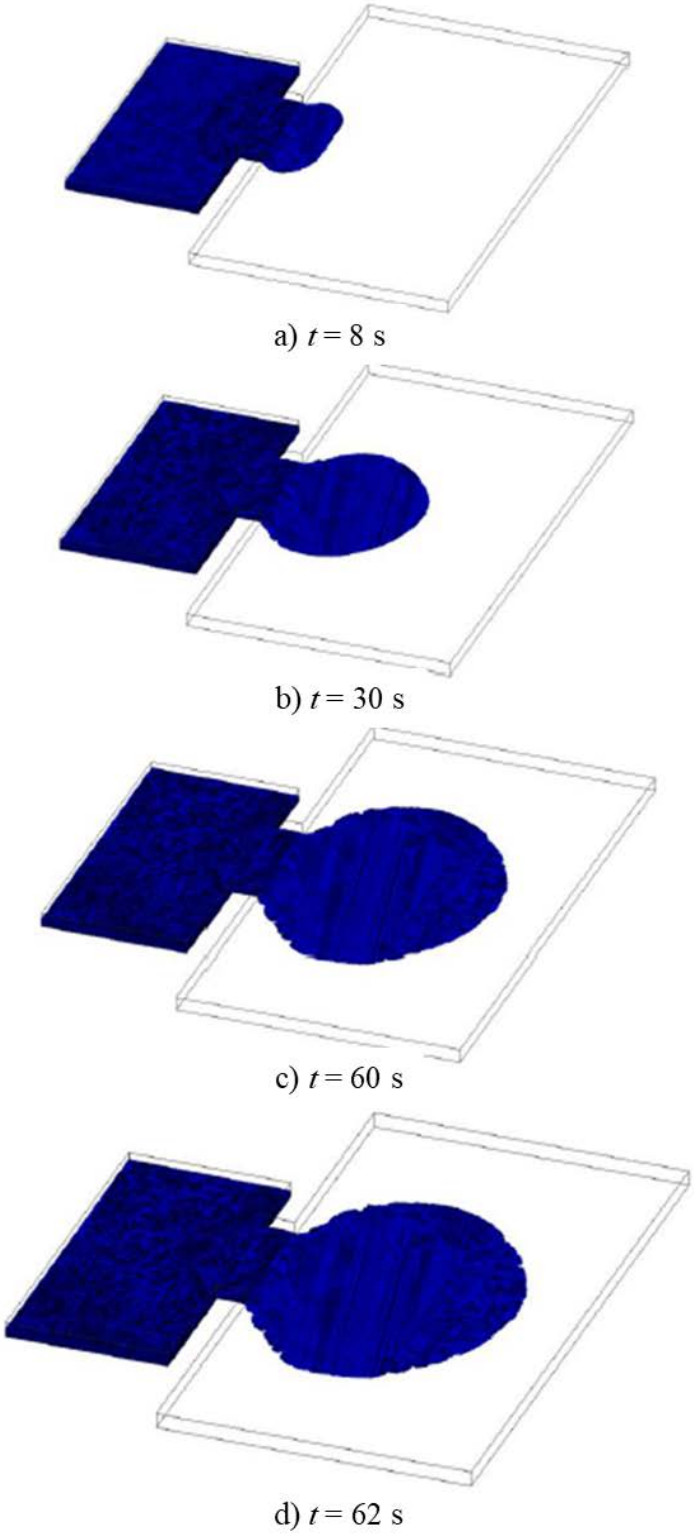

Figure 31. Mining tailings dam. 3D simulation.
Isometric view of evolution of the flow.

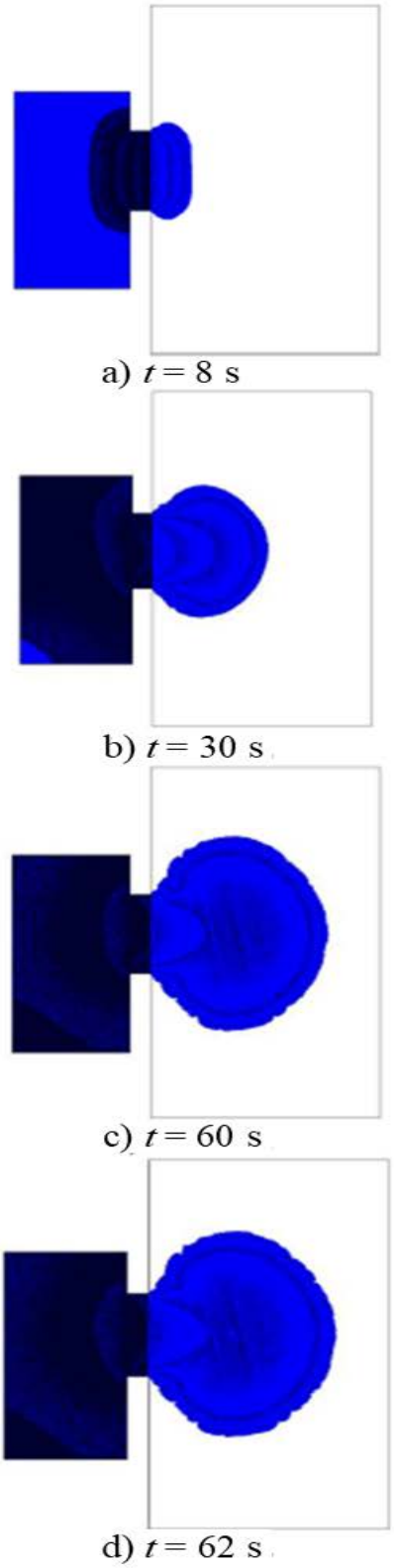

Figure 32. Mining tailings dam. 3D simulation.
Plan view of evolution of the flow.

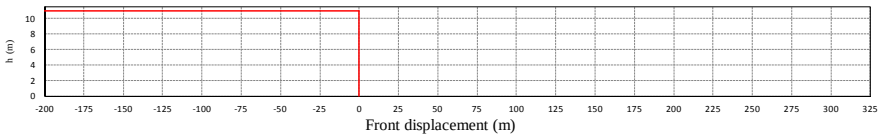

a) t = 0 s.

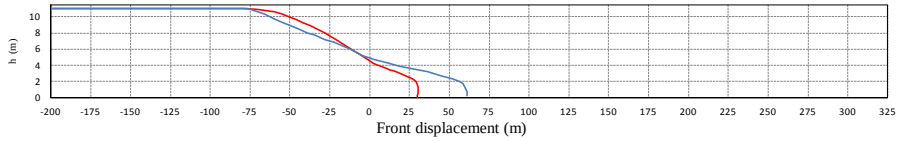

b) t = 8 s

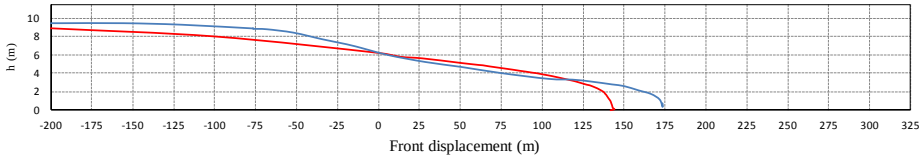

c) t = 30 s

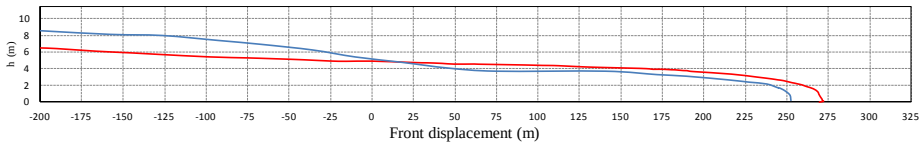

d) t = 60 s

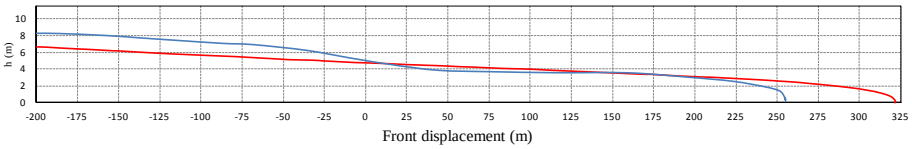

e) t = 62 s (3D), 87 s (2D)

Figure 33. Mining tailings dam. Comparison of the evolution of the free surface Evolution of the free surface in the fluid displacement zone.in the 3D (blue) and simplified 2D (red) simulations.

REFERENCES

[1] LARRAURI P. C., LALL U. 2018 Tailings Dams Failures: Updated Statistical Model for Discharge Volume and Runout, Environments 5(2): 28.

[2] SANTOS J. L., MALVAR J. L., MARTÍN J., APARICIO I., ALONSO E. 2020 Distribution of metals in sediments of the Guadiamar river basin 20 years after the Aznalcóllar mine spill: Bioavailability and risk assessment, Journal of Environmental Management 260(15): 110146.

[3] GALÁN E., GONZÁLEZ I. AND FERNÁNDEZ-CALIANI J. C. 2002 Residual pollution load of soils impacted by the Aznalcóllar (Spain) mining spill after clean-up operations, The Science of the Total Environment external link, 286 (1-3):167-179.

[4] FAN X., TANG C. X., VAN WESTEN C. J., AND ALKEMA D. 2012 Simulating dam-breack flood scenarios of the Tangjiashan landslide dam induced by the Wenchuan Earthquake, Natural hazards and earth system sciences 12(10):3031-3044.

[5] RITTER, A. (ed.) 1892. Die Fortpflanzung der Wasserwellen. Vereine Deutcher Ingenieure Zeitswchrift, 36, 947-954.

[6] STOKER, J. 1957. Water wave. The mathematical theory with aplications, New York, USA, Intersciences Publishers.

[7] MANGENEY, A., HEINRICH, P. & ROCHE, R. 2000 Analytical solution for Testing Debris Avalanche Numerical Models. J. Pure and Applied Geophysics, 157(6)**,** 1081-1096.

[8] FAURE, J. & NAHAS, N. 1961. Etude numérique et expérimentale díntumescences à forte courbure du front. J. La Houille Blanche, 5: 576-586.

[9] CHANSON, H. 2004. Environmental hydraulic of open channel flows, Oxford, UK, Elseiver Butterwortj-Heinemann.

[10] BINGHAM, E. 1922 Fluidity and plasticity. New York: McGraw-Hill.

[11] ANCEY CH., COCHARD S., 2009 The dam-break problem for Herschel-Bulkley viscoplastic fluids down steep flumes, J. Non-Newtonian Fluid Mech., 158: 18–35.

[12] JAY, P., MAGNIN, A. & PIAU, J. 2001 Viscoplastic fluid flow through a sudden axisymetric expansion. Jl. AIChE, 47(10)**,** 2155-2166.

[13] CHHABRA, R. & RICHARDSON, J. 2008 Non-Newtonian flow and applied rheology. Engineering applications, Institution of Chemical Engineering, Elseiver Butterwortj-Heinemann.

[14] SLIJECPČEVIĆ, S. & PERIĆ, D. 2004 Some aspects of computational modelling of non-Newtonian fluids based on stabilized finite element method. Engineering Computations, 18 (34): 577-591.

[15] COUSSOT, P., LAIGLE, D., ARATTANO, M., DEGANUTTI, A. & MARCHI, L. 1998 Direct determination of rheological characteristics of debris flow. Journal of Hydraulic Engineering-Asce, 124(8), 865-868.

[16] LAIGLE, D. & COUSSOT, P. 1997 Numerical modeling of mudflows. Journal of Hydraulic Engineering-Asce,123(7), 617-623.

[17] JEONG, S.W., LOCAT, J. & LEROUEIL, S. 2012 The effects of salinity and shear history on the rheological characteristics of illite-rich and Na-montmorillonite-rich clays. Clays and Clay Minerals, 60(2), 108-120.

[18] WANG W., LI X., HAN X. 2012 Numerical simulation and experimental verification of the filling stage in injection molding Polym. Eng. Sci, 52 : 42-51.

[19] BORZENKO E.I., SHRAGER G.R. 2016 Flow of a non-Newtonian liquid with a free surface J. Eng. Phys. Thermophys., 89: 902-910.

[20] BORZENKO E.I., RYLTSEVA K.E., SHRAGER G.R. 2018 Free-surface flow of a viscoplastic fluid during the filling of a planar channel, Journal of Non-Newtonian Fluid Mechanics 254: 12-22.

[21] NIKITIN K. D., OLSHANSKII M. A., TEREKHOV K. M. AND VASSILEVSKI Y. V. 2011 a numerical method for the simulation of free surface flows of viscoplastic fluid in 3D, Journal of Computational Mathematics 29 (6):605-622.

[22] MORENO, E., LARESE, A. and CERVERA, M., 2016 Modeling of Bingham and Herschel-Bulkley flows with mixed stabilized P1/P1 finite elements using orthogonal subgrid scales, Journal of Non-Newtonian Fluid Mechanics, 228, 1-16.

[23] PAPANASTASIOU, T. 1987. Flow of material with yield. Journal of Rheology, 31(5): 385–404.

[24] CODINA, R. 2002 Stabilized finite element approximation of transient incompressible flows using orthogonal subscales., Comput. Methods Appl. Mech. Eng. 191: 4295–4321.

[25] OLDROYD, J. 1947. A rational formulation of the equations of plastic flow for a Bingham solid Proc. Camb. Philos., Soc. 43: 100-105.

[26] REINER, E. 1958. Rheology, in Handbuch der Physik, edited by S. Flügge, Springer-Verlag, Berlin 6, 434–550.

[27] PRAGER, W. 1961. Introduction to mechanics of continua, Boston, Ginn.

[28] PERIĆ, D. & SLIJECPČEVIĆ, S. 2001 Computational modelling of viscoplastic fluids based on a stabilized finite element method. Engineering computations,18, 577-591.

[29] MITSOULIS, E., ZISIS, TH. 2001 Flow of Bingham plastics in a lid-driven square cavity, Journal of Non-Newtonian Fluid Mechanics, 101(1–3): 173-180.

[30] FREY, S., FILIPE, S. & ZINANI, F. 2010. Stabilized mixed approximations for inertial viscoplastic fluid flows. J. Mechanical Research Comunications, 37: 145-152.

[31] SOUZA, M. P. R. & DUTRA, E. S. S. 2004. Viscosity function for yield-stress liquids. Appl. Rheol., 14, 296 -30.

[32] ASCHER, U. M.; PETZOLD, L. R. 1998 Computer Methods for Ordinary Differential Equations and Differential-Algebraic Equations, SIAM, Philadelphia.

[33] CERVERA, M., CHIUMENTI, M., VALVERDE, Q. & DE SARACIBAR, A. 2003. A mixed linear/linear simplicial elements for incompressible elasticity and plasticity. J. Computer Methods in Applied Mechanics and Engineering, 192 (49-50)**,** 5253-5264.

[34] HUGHES, T.J.R. 1995. Multiscale phenomena: green's functions, the dirichlet-to-neumann formulation, subgrid scale models, bubbles and the origins of stabilized methods, computer methods in applied mechanics and engineering, 127 (1–4): 387-401.

[35] HUGHES, T., FRANCA, L. & HULBERT, G. 1989 A new finite element formulations for computational fluid dynamics: VIII. The Galerkin/least-square method for advective-diffusive equations". Computer Methods in Applied Mechanics and Engineering, 73, 173-89.

[36] CODINA , R. 2001. A stabilized finite element method for generalized stationary incompressible flows. J. Compu. Methods in Applied Mechanics and Engineering,190, 2681-2706.

[37] CODINA, R. 2000. Stabilization of incompressibility and convection through orthogonal sub-scales in finite element methods. Computer Methods in Applied Mechanics and Engineering, 190**,** 1579-1599.

[38] CODINA, R. 2000 On stabilized finite element methods for linear system of convection-diffusion-reaction equations, Comput. Methods Appl. Mech. Eng. 188: 61–82.

[39] COPPOLA-OWEN, H. 2009. A fine element model for free surface and two fluid flows on fixed meshes. Ph. D, Universidad Politécnica de Cataluña.

[40] SETHIAN, J. A. 1999 Level Set Methods and Fast Marching Methods : Evolving Interfaces in Computational Geometry, Fluid Mechanics, Computer Vision, and Materials Science. Cambridge University Press.

[41] BAHBAH C., KHALLOUFI M., LARCHER A., MESRI Y., COUPEZ T., VALETTE R., HACHEM E., 2019 Conservative and adaptive level-set method for the simulation of two-fluid flows, Computers & Fluids, 191:104223.

[42] BIRD, R., ARMSTRONG, R. & HASSAGER, O. 1987. Dynamics of polymeric liquids, Wiley.

[43] KELESSIDIS, V., MAGLIONE, R., TSAMANTAKI, C. & ASPIRTAKIS, Y. 2006. Optimal determination of rheological parameters for Herschel–Bulkley drilling fluids and impact on pressure drop, velocity profiles and penetration rates during drilling. J. of Petroleum Science and Engineering, 53, 203.

[44] NICKELL, R. & TANNER, R. 1974. The solution of viscous incompressible jet and free-surface flows using finite-elemnt methods. J. Fluid mechanics, 65, part 1, 189-206.

[45] TANNER, R. 2000. Engineering rheology, Oxford University Press.

[46] MEZI D., AUSIAS G., GROHENS Y., FÉREC J., 2019 Numerical simulation and modeling of the die swell for fiber suspension flows, Journal of Non-Newtonian Fluid Mechanics,274: 104205.

[47] ELLWOOD, K., GEORGIOU, G., PAPANASTASIOU, T. & WILKES, J. 1990. Laminar jets of Bingham-Plastic liquids. J. of Rheology, 34**:** 6.

[48] IHLE C. F., TAMBURRINO A., 2018 Analytical solutions for the flow depth of steady laminar, Bingham plastic tailings down wide channels, Minerals Engineering, 128: 284-287.

[49] REDDY, K. & TANNER, R. 1977. Finite Element approach to die-swell problem of non Newtonian fluids. Fluid Mechanics Conference. Australia.

[50] CROCHET, M. & KEUNINGS, R. 1982. On numerical die swell calculation. J. Non-Newtonian Fluid Mechanics, 10(1-2):85-94.

[51] ABDALI, S. & MITSOULIS, E. 1992. Entry and exit flows of Bingham fluids. J. Rheology, 36(2): 389-407.

[52] GOREN, S. & WRONSKI, J. 1965. The shape of low-speed capillary jets of Newtonian liquids. J. Fluid mechanics, 25: 185-198.

[53] SCHOKLITSCH, A. 1917. Über dambruchwellen, Sitzungberichten der Königliche Akademie der Wissenschaften, 126, 1489-1514.

[54] JEYAPALAN, J., DUNCAN, J. & SEED, H. 1983. Investigation of flow failure of tailings dams. J. Geothecnical Engineering, 109**,** 172-189.

[55] CHHABRA, R. & RICHARSON, J. 2008. Non-Newtonian flow and applied rheology. Engineering applications, Institute of Chemical Engineering.

[56] DELINGER, R. & IVERSON, R. 2004. Granular avalanches across irregular three-dimensional terrain: Theory and computatation. J. of Geophisical Research, 109.

[57] HERREROS, M. 2004. Desarrollo de modelos numéricos aplicados a hidráulica ambiental. Ph. D., Universidad Complutense de Madrid.